



Dynamics of the Terra Nova Bay Polynya: The potential of multi-sensor satellite observations



Thomas Hollands ^{a,*}, Wolfgang Dierking ^{a,b}

^a Alfred Wegener Institute, Helmholtz Centre for Polar and Marine Research, 27570 Bremerhaven, Germany

^b Arctic University of Norway, 9019 Tromsø, Norway

ARTICLE INFO

Article history:

Received 27 April 2016

Received in revised form 13 September 2016

Accepted 2 October 2016

Available online 10 October 2016

Keywords:

Sea ice

Polynya

Multi-sensor satellite observations

Terra Nova Bay

Microwaves

Thermal IR

Optical images

Ice type classification

Ice drift retrieval

ABSTRACT

Research on processes leading to formation, maintenance, and disappearance of polynyas in the Polar Regions benefits significantly from the use of different types of remote sensing data. The Sentinels of the European Space Agency (ESA), together with other satellite missions, provide a variety of data from different parts of the electromagnetic spectrum, at different spatial scales, and with different temporal resolutions. In a case study we demonstrate the advantage of merging data from different spaceborne instruments for analysing ice conditions and ice dynamics in and around the frequently occurring Terra Nova Bay Polynya (TNBP) in the Ross Sea in the Antarctic. Starting with a list of polynya parameters that are typically retrieved from satellite images, we assess the usefulness of different sensor types. On regional scales (several 100 km), passive microwave radiometers provide a view on the mutual influence of the three Ross Sea polynyas on sea ice drift and deformation patterns. Optical sensors with meter-scale resolution, on the other hand, allow very localized analyses of different polynya zones. The combination of different ranges of the electromagnetic spectrum is essential for recognition and classification of ice types and structures. Radar images together with data from thermal infrared sensors, operated at tens to hundreds of meters resolution, improve the separation of the outlet zone of the polynya from the adjacent pack ice. The direct comparison of radar and passive microwave images reveals the visibility of deformed ice zone in the latter. A sequence of radar images was employed to retrieve ice drift around the TNB, which allows analysing the temporal changes of the polynya area and the extension and structure of the outlet zone as well as ice movements and deformation that are influenced by the katabatic winds.

© 2016 The Authors. Published by Elsevier Inc. This is an open access article under the CC BY license (<http://creativecommons.org/licenses/by/4.0/>).

1. Introduction

In this paper we deal with concurrent multi-sensor satellite observations of a frequently occurring coastal polynya in the Terra Nova Bay, which is located in the Ross Sea/Antarctica. The motivation is to assess the gain that can be achieved in the research of polynya evolution and dynamics when combining data of ESA's different Sentinel satellite missions (e.g., <https://sentinels.esa.int>), which carry various sensors such as imaging radar, multi-spectral instruments, and thermal radiometers. Coastal polynyas are highly dynamic areas of open water and recently formed ice that develop between the coast and the offshore pack ice. From a geoscience and biochemical point of view they are of large interest because (a) they are locations of strong heat and moisture exchange between atmosphere and ocean; (b) cooling effects and the formation of frazil ice cause local density changes and mixing of the water volume below, which are processes that may affect ocean stratification on local and even regional scales; (c) in daylight the biological primary

production is high, and atmosphere CO₂ is sequestered into the ocean by physical-chemical processes (Willmott et al., 2007).

Polynyas occur in ice-covered ocean regions in the Arctic and Antarctic, mostly in inaccessible places. Hence, remote sensing provides an essential tool for gathering data about polynyas. One major question in studies dealing with polynya dynamics is which parameters can be provided by means of remote sensing? Here we address the use of remote sensing data for process studies and parameter retrievals, considering various satellite sensors, which (a) cover a wide range of the electromagnetic spectrum from visible to microwave frequencies, (b) are operated on different spatial scales, and (c) deliver data at different temporal intervals.

Because of their independence from cloud coverage and frequent data acquisitions over a given area, passive microwave radiometers (PMR) are preferred satellite sensors for monitoring polynyas (e.g., Kern et al., 2007; Kern, 2009). Methods have been developed to estimate the polynya area (e.g., Markus and Burns, 1995; Hunewinkel et al., 1998), and the thickness of thin ice that forms in the polynya (Martin et al., 2004; Martin et al., 2005). The polynya extent is directly determined from measured microwave intensity ratios, using thresholds for separating open water and thin ice from thicker offshore pack ice and land or ice shelves (e.g., Willmes et al., 2010). The ice thickness

* Corresponding author.

E-mail addresses: thomas.hollands@awi.de (T. Hollands), wolfgang.dierking@awi.de (W. Dierking).

has to be calculated indirectly using empirical relationships that typically are established by comparison with complementary data, e.g., from infrared sensors. Considering the small width of several polynyas (here, “small” means < 1–10 km), in particular in their early evolution phase, the drawback of satellite PMRs is their coarse spatial resolution (presently between 5 and 40 km, dependent on instrument, frequency, and imaging mode). This leads to contamination effects at the polynya edges (e.g., signal mixtures of land and open water or thin and pack ice). The advantage of PMRs is that variations of polynya extent and thin ice thickness can be continuously monitored in the long term with only small temporal gaps of roughly 24 h, but often less. Recent satellite-borne PMRs are the Advanced Microwave Scanning Radiometer (AMSR-2) on the Japanese GCOM-W1 satellite and the Special Sensor Microwave Imager Sounder (SSMIS) carried onboard the spaceborne platforms of the Defense Meteorological Satellite Program (DMSP). Although operated at similar coverage and spatial resolution, data from scatterometers such as QuikSCAT have only been used occasionally (e.g., Willmes et al., 2010). The coarse-resolution radar backscattering coefficients obtained from QuikSCAT are more difficult to interpret in terms of polynya extent and ice thickness since they are also very sensitive to ice surface roughness variations. Hence, QuikSCAT data are of minor importance for the development of robust retrieval algorithms.

Despite their sensitivity to the presence of clouds, the usefulness of thermal infrared (TIR) images for the retrieval of polynya size and thin ice thickness has also been demonstrated in several studies (e.g., Willmes et al., 2010; Krumpen et al., 2011; Ciappa et al., 2012). In maps of surface temperature, cold ice and warmer open water can often be easily separated. For the estimation of thin ice thickness, a thermodynamic ice growth model is employed for which the surface temperature has to be provided as input parameter (e.g., Yu and Lindsay, 1996; Krumpen et al., 2011). Major differences between the temperature in the TIR- and the microwave-regime arise because the former is influenced by a very thin skin layer (for saline water, e.g., the thickness varies between 1 μm and 1 mm for wavelengths between 2 and 16 μm), whereas the latter is determined by layers of 0.04–0.5 cm in thickness (frequencies between 1 and 20 GHz). One advantage of TIR-data is that they are available at high spatial resolution, typically on the order of 1 km and better, and that they are operated at large swath widths, which decreases the time between acquisitions over a given polynya (e.g., the swath width of the Moderate Resolution Imaging Spectroradiometer MODIS is 2330 km compared to 1445 km for AMSR-E).

As complementary data source to TIR-imaging, synthetic aperture radar (SAR) sensors provide an even better spatial resolution between <10 m and 150 m, dependent on radar frequency and imaging mode. Since they are operated at microwave frequencies, their advantage is that they deliver data independent of cloud coverage and daylight – in contrast to optical (“visible range”) sensors which otherwise can be operated at comparable spatial resolutions. At present, Earth Observation (EO) satellite SAR systems operate at frequencies between 1.2 GHz (L-band) and 10 GHz (X-band), and use different polarization combinations (mostly of linear type: HH, HV, VH, VV, with H-horizontal, V-vertical, the first letter indicating the transmitted, the second the received polarization). SAR images have been applied for validating algorithms derived for PMR- and TIR-sensors (e.g., Willmes et al., 2010; Ciappa and Pietranera, 2013; Morelli and Parmiggiani, 2013). Also optical images or aerial photography are useful in this context (e.g., Willmes et al., 2010). Haarpainter et al. (2001), who developed a model for simulating the evolution of the Storfjorden polynya (Svalbard), took time series of SAR images acquired by the European Remote Sensing (ERS-2) satellite for manual classification of sea ice types. Besides variations of polynya shape and size, also ice drift can be determined from sequences of optical or SAR images (e.g., Drucker et al., 2003). The major problem with past satellite SAR missions was that data acquisitions over polynya sites were only irregular and with large time gaps. Constellation missions such as Sentinel-1 and Sentinel-2, consisting of two or more

satellites, significantly reduce the temporal gaps between data acquisitions. It has also to be noted that the swath widths of SAR systems are limited between a few tens and 500 km.

In the studies mentioned above several problems were recognized regarding limitations of the sensor's capacity to provide certain information and parameters. For realistic simulation of, e.g., polynya width and ice production rate, the extent of the open water and thin ice areas as well as the thin ice thickness distribution have to be determined with high accuracy. This is difficult to achieve at coarse spatial resolution and/or insufficient signal contrast between open water and different ice types. One example is the misinterpretation of PMR signals since ice shelves, icebergs, fast ice and thin ice have similar microwave characteristics, and their locations at a given test site change continuously due to calving, breakup and drifting. TIR-data are often considerably influenced by atmospheric conditions. The physical properties of sea ice found in one region may differ from those of sea ice in other regions; hence automated algorithms for parameter retrieval from satellite data, developed for one local test site, cannot be applied globally in every case. In the single-frequency single-polarization SAR images used hitherto, the highly variable signals backscattered from thin ice (bare, rafted, covered with frost flowers) complicate its automated separation from open water and pack ice.

Based on the references cited above, the conclusions regarding future satellite observation strategies over polynyas are:

- Concurrent data acquisitions using complementary sensors (optical, thermal, radar) improve the segmentation and classification of different zones in and offshore from a polynya.
- Regional and local interaction mechanisms at sites of frequent polynya occurrences require satellite images with different spatial coverage and resolution (e.g., PMR versus SAR).
- A higher data acquisition frequency is needed for sensors providing images with high spatial resolution in order to resolve the dynamics of local processes.

In this study, we analyse examples demonstrating the potential of the most recent and future satellite missions for improved monitoring of polynyas and for the retrieval of parameters characterizing polynya evolution. Other examples for the use of data from multiple sensors for studies of polynya dynamics are provided, e.g., in Ciappa and Pietranera (2013), Willmes et al. (2010), or Drucker et al. (2003). They focus in particular on the retrieval of geophysical parameters. In our study, we also pay attention on the usefulness of image processing techniques that can be regarded as preparatory step to increase the robustness and reliability of retrieval algorithms. In Section 2 we give a brief overview about polynya parameters that can be retrieved from remote sensing data. We introduce the background about how those parameters have been used to analyse polynya processes, to simulate their opening and closing, and to estimate ice production rates. The motivation is to provide the reader, who is not familiar with the requirements of polynya research, with the information necessary to assess the pros and cons of different satellite sensors and retrieval methods. Section 3 deals with the local and regional environmental conditions in and around our test site, the Terra Nova Bay, and Section 4 provides information about the satellite data we used for our analyses. We demonstrate the gain of combining different image types for a qualitative analysis of ice conditions in Section 5. Multi-sensor ice classification is discussed in Section 6, and the determination of ice drift and deformation patterns is dealt with in Section 7. At the end we provide a discussion of additional aspects to be considered, followed by the conclusions.

2. Polynya parameters obtained from remote sensing

In this section we provide examples of polynya parameters that have been directly retrieved or indirectly determined from observations

using remote sensing techniques. The purpose of retrievals is to provide parameters for describing the long-term dynamics, climatology, and associated changes of a polynya (e.g., Kern, 2009), to compare observations with model simulations (e.g., Hollands et al., 2013) or to determine parameters that are needed for running the models (e.g., Drucker et al., 2003).

According to Willmott et al. (2007) one distinguishes two major approaches for modelling the evolution of a polynya. These are flux models and general circulation models. The former are based on the assumption that a wind-generated coastal polynya attains a maximum size, which is determined by the balance between the ice production in the open water zone and the flux of the offshore pack ice out of the polynya. The advantage of flux models is that it is easier to identify single dominant processes that influence polynya development. However, it is extremely difficult to incorporate all possible feedback mechanisms, which are more or less well integrated in ocean circulation models including dynamic-thermodynamic sea ice components (e.g., Hollands et al., 2013). Ice concentration, thickness, and drift velocity are among the prognostic variables of such models. The polynya is then defined as an area for which the ice concentration is below a certain threshold (Willmott et al., 2007).

2.1. Polynya area

The most obvious variable that can be retrieved from satellite imagery is the extent of the polynya. Besides being an essential parameter related to polynya formation, evolution and decay, this information is needed to validate simulations both with flux and circulation models, and for tuning coupled polynya - atmospheric models or numerical simulations of the thermohaline circulation induced by polynyas (Ciappa et al., 2012). With knowledge of the polynya extent it is in principle possible to quantify heat losses, new ice production and salt fluxes. When using data from PMR, the simplest method is to define a threshold for the ice concentration, below which the corresponding resolution cell is regarded part of a polynya (e.g., Morelli and Parmiggiani, 2013). This corresponds to the delimitation of polynyas in simulations carried out with circulation models (see above). Another possibility is to employ the polynya signature simulation method (PSSM) to separate thin ice, open water, and thick ice (Markus and Burns, 1995; Kern et al., 2007; Kern, 2009; Willmes et al., 2011; Adams et al., 2013). The polynya extent is then the sum of the thin ice and open water areas. Kern et al. (2007) compared results obtained from the PSSM applied to SSMI data (89 GHz and 37 GHz channels with spatial resolutions of 15 km × 13 km in the former and 37 km × 28 km in the latter case) with ice concentration estimates from AMSR-E 89 GHz data (spatial resolution 6 km × 4 km). They found that AMSR-E ice concentrations of 25–40% corresponded to areas classified as open water using the PSSM, and concentrations of 65–80% were found for areas of PSSM class “thin ice”. (Note that the theoretical concentrations are 0 and 100%, respectively). Kern et al. (2007) explained this with the different frequencies and spatial resolutions used for the estimation and classification. The result demonstrates the need of achieving more detailed spatial information about the ice conditions in and around a polynya.

Because of their high-resolution modes, SAR, optical and TIR sensors enable more subtle analyses of ice conditions especially for smaller polynyas (widths < 10 km) and the separation of open water, frazil and grease ice, closed thin ice, and the offshore pack ice (Dokken et al., 2002; Willmes et al., 2010; Ciappa and Pietranera, 2013; Hollands et al., 2013). Examples from our study will be presented below. In the case of SAR images, visual classification is achieved by considering the backscattered radar intensity and image texture, which are related mainly to the ice surface structure on scales between a few millimeters to centimeters (“small-scale” surface roughness) and 10s of meters (e.g., ice ridges, rafting zones). In the case of low salinity ice, the influence of volume inclusions and structure has also to be taken into account. Temperature variations are related to thickness changes

between different ice growth stages or ice types. Williams et al. (2007), their Fig. 1) distinguish four different measures of the polynya width, namely (1) the region of open water, (2) the region of open and partially open water, (3) the “practical width” which encompasses all ice cover which is too thin for safe travel, and finally (4) the “full width” which includes all ice that is thinner than the offshore pack ice. The degree of details that can be achieved in separating different zones depends not only on spatial resolution but in the case of SAR, e.g., also on the frequency and polarization.

2.2. Polynya and coastline shape

A more comprehensive look at polynya evolution requires considering the shape of the coastline in front of which the polynya is located. Besides of the orientation of single coastline segments, the steady state shape of a coastal polynya (more precisely of its offshore open-water edge) is influenced by magnitude u and direction α of the movement of free-drifting frazil ice, and by magnitude U and direction θ of the consolidated thin ice in the polynya (e.g., Darby et al., 1995; Krumpen et al., 2011, their Fig. 2). Darby et al. define an along-shore length scale L_C on which the polynya adjusts to its steady-state width (see their Fig. 2 explaining the practical determination of L_C). This parameter depends both on θ and α . Coastline variations that are shorter than L_C are not mirrored in the shape of the open-water edge. The magnitude of L_C can vary between zero and tens of kilometres (Darby et al., 1995). Hence satellite images with spatial resolutions on the order of 100 m and less and with a clear accentuation of the coastline and the open-water edge are needed. Darby et al. (1995) presented simulations for the Terra Nova Bay Polynya with the actual coastline geometry, which revealed a realistic shape of the open-water edge.

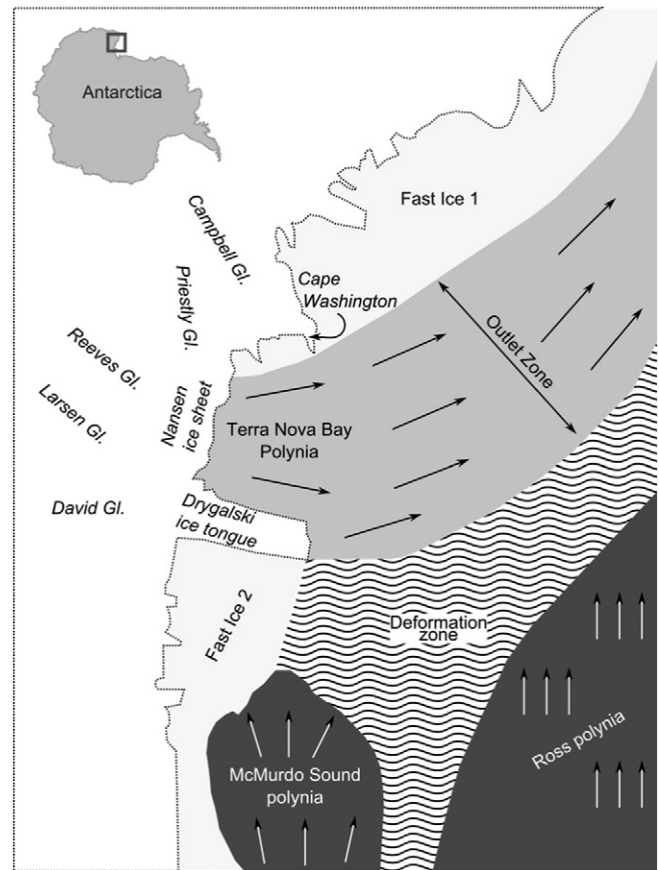


Fig. 1. TNBP and adjacent regions, showing major sea ice zones with dominant drift directions and locations of the outlet glaciers mentioned in the text.

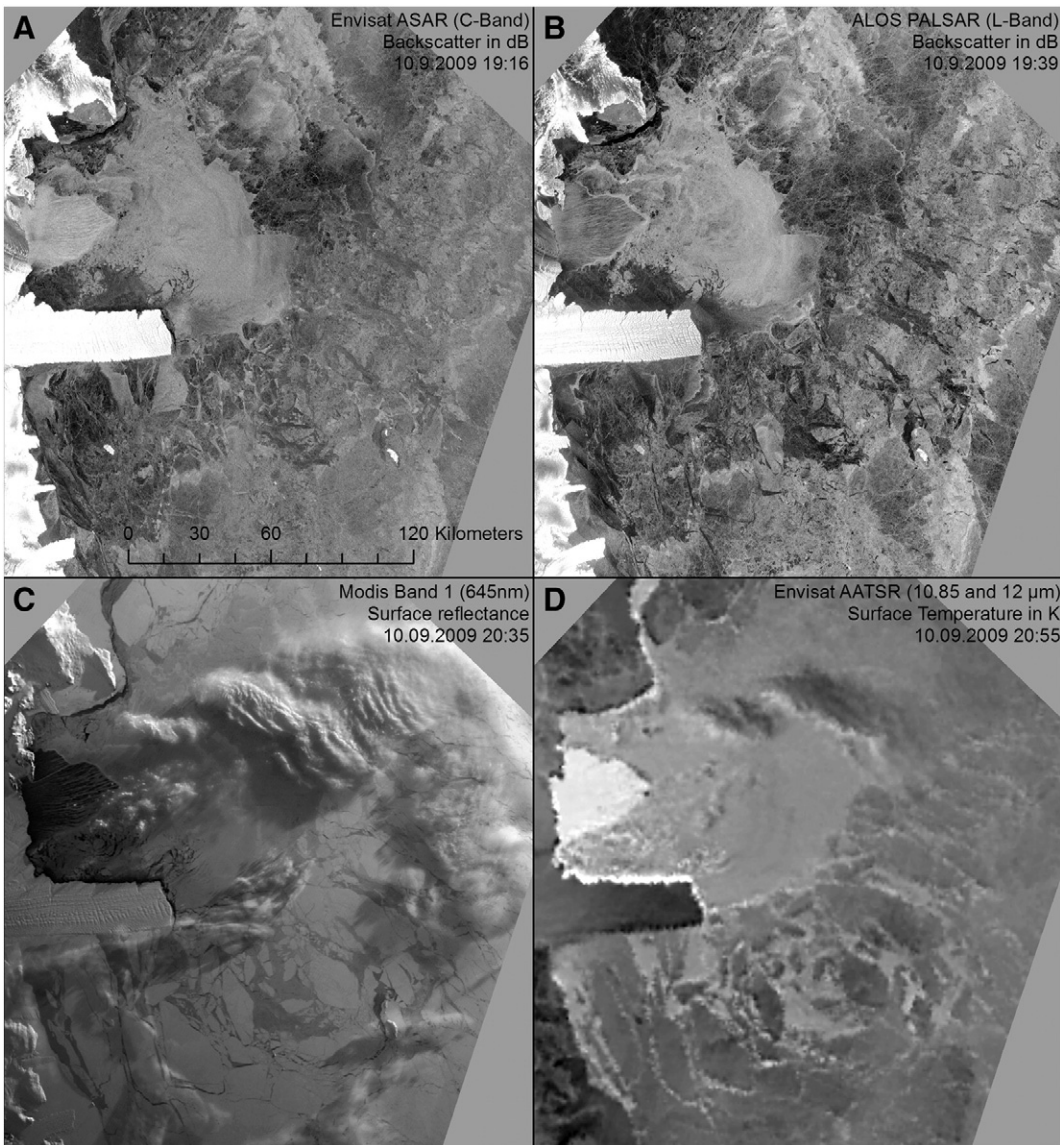


Fig. 2. Satellite images showing the local environment around the TNBP. The respective sensor with acquisition date and timing is given in the upper right corner of each image, the coverage is about 150 km × 150 km.

2.3. Ice production rate

From a geophysical point of view, ice production rates in polynyas are the most interesting parameter since they have to be taken into account for estimating variations between ice production in a given area and ice transport out of this area. The estimation of ice formation requires to determine the size of the polynya (or – better – of the different water and ice zones in the polynya, see above) and to retrieve the ice thickness. The surface heat loss and ice volume production can be calculated if corresponding meteorological data are available (e.g., Willmes et al., 2010; Krumpen et al., 2011). Underlying assumptions are that the sum of radiative and turbulent fluxes at the ice surface is balanced by the conductive heat flux in the ice, that all heat loss at the surface is used for ice formation, and that the oceanic heat flux is small. The latter is often valid in polynyas because the whole water column is close to the freezing point during winter in the continental shelf region (Tamura et al., 2008). The use of TIR and PMR for ice thickness retrieval and their pros and cons were mentioned in the introduction above. Using TIR, good results can be obtained for ice thicknesses below 0.5 m, if the vertical temperature profile in the ice is linear and the ice is snow-free (Drucker et al., 2003). A large source of errors arises from uncertainties

in the meteorological data (Willmes et al., 2010). When using PMR, the distinction of different ice thickness classes is hampered due to the coarse spatial resolution of those sensors (Willmes et al., 2010, their Fig. 7). The validation of thickness retrievals over thin polynya ice is extremely difficult, even with airborne instruments such as electromagnetic probes since their measurement uncertainty is too large (Willmes et al., 2010). In summary, the estimation of ice thickness and ice production rates from remote sensing data and their validation remain very challenging.

2.4. Ice formation, drift, and deformation

As mentioned above, drift velocity and direction of frazil and consolidated polynya ice are required in flux models (e.g., Darby et al., 1995; Krumpen et al., 2011). The ice drift is a prognostic variable of circulation models (e.g., Hollands et al., 2013). While the drift of frazil ice in the open water area of polynyas cannot be retrieved with recent satellite systems, this is often possible for consolidated polynya and offshore pack ice. Different retrieval algorithms are available that can be applied on sequences of satellite images (SAR, TIR, VIS). One of the most popular approaches is a multi-scale multi-resolution pattern matching

algorithm requiring an image pair as input, which was used by Hollands et al. (2013) and results in acceptable accuracies of 3 to 5 pixels for the retrieved displacement vectors during freezing conditions (Hollands and Dierking, 2011). However, the approach requires recognizable radar signature variations on different spatial scales that can be found in both the first and second image (see next paragraph). The relatively large temporal gap between both images (rarely less than one day with most recent SAR systems when operated in high-resolution imaging mode) is often a problem considering the fast changes of ice conditions offshore from evolving polynyas. The temporal acquisition rate is higher with recently launched or planned satellite constellations (such as Cosmo Skymed, Sentinel-1, Radarsat Constellation).

In their analysis of the Pease model, e.g., Drucker et al. (2003) employ SAR data to determine the advection of the pack ice away from the polynya region. Also using SAR imagery, Hollands et al. (2013) retrieved the drift velocities of consolidated thin ice and of pack ice in the Ronne Polynya area located in the Weddell Sea. They note that the accuracy depends critically on the presence of recognizable ice structures, which may be buried under wet snow during melting conditions, or may change very quickly because of strong movements and deformations of newly formed ice in the polynya. In both cases, the retrieved ice velocities are less reliable than for the offshore pack ice under freezing conditions.

Gallée (1997) used a coupled atmosphere – polynya model to study the air-sea interactions over the Terra Nova Bay Polynya in winter. He pointed out that there is a need for having a better knowledge of frazil ice evolution (consolidation of frazil into pancakes, frazil herding). In his model he used a simple cavitating fluid behaviour for the sea ice rheology in the polynya, which means that the “model ice” reveals divergence or shear but does resist convergence. Hence the effects of ridging and rafting are not included in the simulations.

3. Terra Nova Bay

3.1. Large scale situation

In the Antarctic Ocean, the Ross Sea Polynya (RSP) is the largest polynya with a winter area of around 20,000 km² (Barber and Massom, 2007, their Table 23). Two smaller polynas are located in the western part of the Ross Sea, one in Terra Nova Bay (the Terra Nova Bay Polynya, in the following denoted as TNBP, with a mean area of 1300 km² and maxima up to 5000 km² (Van Woert, 1999)) and the other in the McMurdo Sound (MSP, with an area about 2/3 of TNBP, see Kern (2009), Table 2). Tamura et al. (2008) found that the highest ice production of the Antarctic Ocean occurs in the Ross Sea. From the 1990s to the 2000s, the ice production (in volume) decreased by about 30% due to a decrease in polynya areas and due to atmospheric warming. Tamura et al. (2008) suppose that the negative trend in ice production is one reason for the recent freshening of the Antarctic Bottom Water. Drucker et al. (2011) report that the ice production in the Ross Sea approximately equals the ice export. The former was estimated from 36 GHz AMSR-E data, the latter was calculated for flux gates parallel to the 1000-m isobaths, using maps of daily ice motion retrieved from 89 GHz AMSR-E data. From 2003 to 2008, the average annual ice production of the RSP amounted to 510–730 km³, of the TNBP 70–111 km³, and of the MSP 11–80 km³ (numbers are given per freezing season). The total ice production in these three polynyas accounts for 20% to 50% of the total sea ice volume in the Ross Sea.

3.2. Local conditions in Terra Nova Bay

The coastal polynya in Terra Nova Bay is oriented in east-west direction. It is bounded by the Drygalski Ice Tongue in the south and by the Campbell Ice Tongue in the north (see Fig. 1). The polynya is generated and maintained by persistent katabatic winds with speeds of up to > 40 m/s, which push the bay ice offshore. The katabatic wind field is a

complex mixture of different branches from Larsen, Reeves, Priestly and David Glacier. The Drygalski Ice Tongue, which is an extension of the David Glacier, blocks northward drifting sea ice that originates from McMurdo Sound and the coast of Ross Island. Hence, the length and orientation of the ice tongue influences shape and size of the TNBP. Rusciano et al. (2013) separate two different stages of polynya activities: increasing and decreasing ice production in March–June and December–February, respectively, and a period of maximum efficiency in sea ice production from July to November. The open water area of the TNBP during winter time estimated from TIR-data ranges from 1000 to 1300 km² (but peaks of 8500 km² were observed). The combined open water and thin ice area obtained from PMR is larger by a factor of about 2 (Ciappa et al., 2012). Ciappa and Pietranera (2013) characterize the different phases of polynya evolution. When the ice is pushed away from the coast (opening phase), frazil ice that is organized as ice streaks parallel to the wind direction occurs in the open water area. Using high-resolution SAR imagery, Ciappa and Pietranera (2013) measured distances between the streaks ranging from 300 to 800 m. They also recognized waves of lengths between 30 and 70 m, which modulated the streaks and the frazil and grease ice accumulated at the offshore polynya margin. When the wind speed decreases, the gaps between the streaks become smaller. Progressive freezing from the offshore edge of the polynya to the coast characterizes the closing phase. This suggests that the detection of the polynya area with IR-sensors or PMR is more reliable during the growing phase, when large areas of unfrozen water are present, than during the closing phase when large areas of thin sea-ice prevail.

Gallée (1997) states that the polynya size is poorly correlated with the large-scale wind forcing, suggesting that its main forcing is the katabatic wind. Regional ice conditions are influenced by winds blowing across the Ross Ice Shelf (Van Woert, 1999). Gallée (1997) found that the open warm water area significantly influences the atmospheric circulation in the coastal zone. Morelli and Parmiggiani (2013), who combined satellite observations and model simulations, obtained a similar result, which reveals that the heating of the air associated with the polynya increases the speed of the katabatic wind over the polynya after it has crossed the coastline. This, in turn, is in line with the study by Van Woert (1999) who showed that changes of sensible and long-wave heat fluxes can explain up to about 50% of the observed variance in the polynya open water fraction. Different stages of cloudiness can explain another 8–10% of the variance. Ciappa et al. (2012) found most cloudy periods during phases of limited polynya activities at low wind conditions. Fluctuations of the open water area can occur within very short time intervals in the order of hours, and peaks of areal growing rate may exceed 300 km² during extreme wind gusts (Ciappa and Pietranera, 2013).

TIR images can be used to analyse the variability of strong surface winds (Bromwich, 1989) over snow-covered regions. The images may reveal delimited warmer areas indicating the presence of strong katabatic airstreams. The reason why those airstreams manifest themselves in the thermal signature is the intense vertical mixing of the air and drifting snow. Inland from the coast of Terra Nova Bay Ciappa et al. (2012) recognized the signatures of katabatic winds descending from the glaciers flowing towards the bay. They found that when the polynya is open, airflow from the Reeves Glacier is always strong. The opening is large when surface winds of the other three glaciers contribute to the katabatic wind flow originating from the Reeves Glacier. Because of this complex airflow structure, it is difficult to explain the TNBP evolution using a one-dimensional flux model, instead, a 2-dimensional model is needed.

4. Data

The data that we used for our analysis were acquired over the TNBP in September 2009 (Table 1). The dataset consists of high- and coarse-resolution imagery. The former includes SAR data (ALOS PALSAR,

Envisat ASAR), optical data from EO1-ALI (Earth Observing 1 Mission Advanced Land Imager, in the following ‘optical’ is used synonymously with ‘visible range’), MODIS optical and near-infrared (NIR), AVHRR (TIR), and AATSR thermal (TIR) images. Coarse-resolution products are from a passive microwave radiometer (PMR), namely AMSR-E. Details about sensors and images are provided in [Table 2](#). In particular for September 10, 2009, favourite conditions for inter-comparisons of different sensors are given since PALSAR, ASAR, AATSR, MODIS, and EO1-ALI data were all acquired within a short temporal window.

The ASAR and PALSAR data were geocoded and calibrated using the commercial SARscape software. The high-resolution data were re-projected to an Antarctic Polar Stereographic Projection with a Central Longitude of 180° E and a Standard Latitude of 71°S. If comparisons of fixed targets (e.g., coastlines and islands) revealed slight discrepancies, the respective images were co-registered to the corresponding Envisat ASAR scene. All images were resampled to a resolution of 100 m × 100 m.

Both AVHRR and AATSR sea surface temperature (SST) temperatures are based on the combination of the 11 μm- and 12 μm-band. The AVHRR SST was evaluated following [Key et al., 1997](#). For the calculation of the AATSR SST the ESA VISAT Software was used. In contrast to AVHRR, the AATSR sensor acquires one image in forward direction (looking slanted through the atmosphere) and a second one nadir-looking, in order to compensate for atmospheric effects in the calculations of the SST ([ESA, 2002; Corlett et al., 2006](#)). The comparison of the AVHRR and AATSR data showed variable differences on a point-to-point scale (which is partly caused by ice movements in the time interval of 2 h between data acquisitions). On average the data compared well, allowing solid conclusions in the frame of our analysis.

The high-resolution images were supplemented by AMSR-E 89 GHz data for the period September 5–12, both at original and at spatially enhanced resolution (the data set that we used is described in [Long and Stroeve, 2011](#)). In contrast to the spatial resolution of 5.4 × 5.4 km/pixel in the original 89 GHz data, the spatially enhanced version has a resolution of 2.2 × 2.2 km. In enhancement algorithms, the antenna pattern is de-convolved for reconstruction of the underlying brightness temperature distribution on a higher-resolution grid. Resolution-enhancement techniques, however, provide improved resolution at the expense of an increased noise level ([Long and Daum, 1998](#)). Nevertheless, the enhanced images allowed the identification of more details in the area around the polynya. We use the brightness temperature data as obtained, without considering any atmospheric effects that influence high frequency bands like the employed 89 GHz channel.

5. Qualitative analyses of polynya conditions

With our dataset it is possible to carry out qualitative analyses including the following elements:

Table 1

Satellite images used for the case study presented in [Sections 5–7](#). Sensor abbreviations are explained in the text.

Date	Time (UTC)	Sensor
06.09.2009	19:41:47	Envisat ASAR WS Scene
07.09.2009	19:10:28	Envisat ASAR WS Scene
07.09.2009	21:19:36	EO1 ALI
09.09.2009	19:47:34	Envisat ASAR WS Scene
10.09.2009	12:39:57	Envisat AATSR Scene
10.09.2009	19:16:19	Envisat ASAR WS Scene
10.09.2009	19:39:20	ALOS PALSAR ScanSAR
10.09.2009	20:35:00	MODIS
10.09.2009	20:55:37	Envisat AATSR Scene
11.09.2009	20:19:36	ALOS PalSAR ScanSAR
11.09.2009	20:24:20	Envisat AATSR Scene
Daily (5.–12.9.2009)		AMSR-E 89GHz –Horizontal
Daily (5.–12.9.2009)		AVHRR

- separation of ice types and structures in and adjacent to the polynya on local scale employing near-simultaneously acquired imagery with high spatial resolution from SAR, TIR, and optical sensors,
- interpretation of regional ice cover characteristics a few 100 km around the polynya, based on PMR-data, and linking local to regional conditions,
- monitoring of the polynya evolution and of variations of polynya parameters such as its size, shape, or relative areal fractions of different zones (i.e. open water, frazil ice herding, accumulated and/or consolidated ice).

When combining data from different ranges of the electromagnetic spectrum one has to consider the sensitivities of the respective measured quantity (brightness temperature T_B , backscattering coefficient σ^0 , temperature T , reflectivity R) to the physical properties of the imaged area. Sensitivities to sensor configurations, such as e.g., frequency, polarization, or direction of measurement, have to be taken into account as well.

5.1. Local analysis

High-resolution SAR and AVHRR images are, e.g., used in the study by [Massom et al. \(2001\)](#) for analysing the ice conditions around the Mertz Glacier Polynya. In [Fig. 2](#), multi-sensor data acquired over the Terra Nova Bay are shown: A – Envisat ASAR, B – ALOS PALSAR, C – MODIS Band 1, and D – Envisat AATSR, covering an area of 22,500 km², with spatial resolutions between 100 m (PALSAR) and 1 km (AATSR). The temporal difference between the first and last data take is 1:39 h. Major structures of the ice cover can be identified in the images, e.g., the coastline, the land ice, the ice tongue, the open water area of the polynya, and single smaller and larger ice floes (compare also to [Fig. 1](#)). The ice formed in the polynya is first exported towards east but then is deflected northeast. We term this band of ice export “outlet zone”. In the visible range (MODIS Band 1), major parts of the outlet zone are covered by clouds. Ice floes appear light grey, and thinner ice areas dark grey. In particular the belt starting south of the Drygalski ice tongue and then gradually turning towards northeast is characterized by heavily broken ice, consisting of smaller and larger thicker floes (light grey) and thin ice. We term this zone “deformation belt”. It is carried away to the east due to shearing forces imposed by the ice in the outlet zone of the TNBP and pushed to the north by the ice originating from the RSP and the MSP (compare [Fig. 1](#)). Smaller clouds are visible over different parts of the scene. The dark area above the Drygalski tongue is the open water zone of the TNBP, with streaks of frazil ice weakly showing up towards the sea ice edge to its right. The thermal image ([Fig. 2D](#)) reveals a coarser spatial resolution but resembles the MODIS scene in major parts. The cloud cover can less clearly be distinguished. Most presumably the distribution of clouds changed in the 90 min between the acquisitions of MODIS and AATSR data. The open water zone appears very bright. It is the area with the highest temperature in the region. The streaks of frazil ice are hardly visible, which may be partly attributable to the coarser spatial resolution of the thermal data, but most probably indicates that the temperature difference between the forming ice crystals and the water at the surface is very low. The ice in the outlet zone of the TNBP is warmer than in the adjacent ice zones, which means that it is relatively thin. Also the thin ice areas in the deformation belt appear bright. Compared to the reflectance ([Fig. 2C](#)) or radar brightness ([Fig. 2, A and B](#)), the temperature variations seem to be most suitable for delimiting the outlet zone. In the SAR images, also the ice under the cloud-covered areas is visible. The information content of the C- and L-band image is similar, but the ice cover structure is more pronounced at L-band. This is more a consequence of the signature contrasts of different ice types and structures than of the different spatial resolutions (PALSAR 100 m, ASAR 150 m). The appearance of the open water zone depends on the radar frequency

Table 2

Specifications for the sensors listed in Table 1.

Sensor	Wavelength	Frequency	Swath width	Spatial resolution	Parameter
Envisat ASAR WS	5.62 cm	5.33 GHz (C-Band)	400 km	150 × 150 m	Backscattering coefficient [dB]
ALOS PALSAR ScanSAR	23.61 cm	1.27 GHz (L-Band)	250–350 km	100 × 100 m	Backscattering coefficient [dB]
AMSR-E 89 GHz, H-polarization		89 GHz (W-Band)	1445 km	5.4 × 5.4 km (2.2 × 2.2 km after enhancement)	Brightness temperature [K]
Modis Band 1	620–670 nm		2330 km	250 × 250 m	Reflectance
Modis Band 2	841–876 nm		2330 km	250 × 250 m	Reflectance
AATSR	3.7, 10.8, 12 μm		512 km	1 × 1 km	SST [K]
AVHRR	0.58–12.5 μm		2900 km	1.1 × 1.1 km	Radiance/SST [K]
EO1 ALI	0.433–2350 μm (7 bands) 0.48–0.69 μm panchromatic		37 km	30 × 30 m (10 × 10 m panchromatic)	Reflectance

and on wind speed and direction. At L-band (Fig. 2 B), a rim is clearly visible at the sea ice edge east (to the right) of the open water area of the TNBP, which is more difficult to identify in the other images (A, C, D). We interpret this rim as a narrow zone of accumulating frazil ice. In both radar scenes, the streaks of frazil ice in the open water zone of the TNBP are recognizable. Thin smooth ice (darker in the radar imagery) and thicker ice floes (brighter) can be better distinguished at L-band. The outlet zone reveals alternating bright, partly banded ice zones, and dark zones consisting of broken level ice. From this structure and the available sequence of SAR images we conclude that relatively smooth level ice zones develop in the polynya area at phases of calm wind and break due to external forces exerted by the adjacent ice masses, while being pushed to the northeast when the katabatic winds increase in strength. The bright zones, with large parts of fine-grained image texture, are characteristic for rough ice surfaces. Based on pairs of SAR images (revealing similar grey-tone patterns) and high-resolution optical images acquired on other days, we assume that these bright areas consist of accumulated frazil and grease ice at the open water margin that is consolidated at larger distances from the open water zone, eventually forming a heavily rafted ice cover and broken ice floes. The banding is then due to different stages of compaction and/or surface roughness. The dark ice area in the upper left corner of both SAR images is fast ice (confirmed by our analysis of a sequence of SAR images discussed below).

Another example is shown in Fig. 3, in which a high-resolution (10 m) EO1 ALI image is superimposed on an ASAR scene. The former was acquired 2:09 h later than the latter. The optical data reveal the organization of frazil and grease ice as streaks. Wind generated waves travel through the streaks (zoom-in, Fig. 3), which was also recognized by Ciappa and Pietranera (2013) in high-resolution (5 m) COSMO SkyMed SAR images. In our wide-swath ASAR scene with a spatial resolution of 150 m, the ice streaks are also visible, although more difficult to identify. The location, width, and shape of individual streaks can change within minutes dependent on local wind conditions. Hence, they do not match perfectly between the ALI and the ASAR image considering the time interval between their acquisitions.

According to Ciappa and Pietranera (2013) the gaps between the streaks depend on wind speed. Lacking satellite photos taken for different wind speeds, we cannot examine this dependency. The ice streaks are unveiled by Langmuir circulation. Thorpe (2004) reports that the separation scales and lengths of Langmuir cells increase with wind speed. In experimental studies it has been observed that there is a tendency for larger spacing between the streaks with higher wind speeds (Plueddemann et al., 1996, their Fig. 5), but there are also clear deviations from this relationship. One reason is that Langmuir circulation does not only depend on the wind stress but also on the Stokes drift (average velocity of a fluid parcel) of surface waves. In our scene, the streaks in the northern part are broader. The width of individual streaks

and their distance to one another increase with the distance from the coast. Morelli and Parmiggiani (2013) point out that the wind speed is larger when moving away from the coast because of the heat released by the open water zone of the polynya. Considering the results of experimental studies on Langmuir circulation just mentioned above, the increasing distance between streaks and their broadening conforms to the wind speed increase with distance from the coast.

In Fig. 4, the ice and water surface temperatures in the Terra Nova Bay for September 10, 2009, derived from AVHRR data, are pictured. We here selected AVHRR and not AATSR data since for that date the former provide a better spatial coverage of the southwest part of the Ross Sea, which we take advantage of in the analysis presented in Section 5.2. The locations of automated weather stations are indicated by red triangles. For the day of the AVHRR data acquisition, the local air temperatures measured at 2 m height above surface at the stations were: Laurie II: −44.6 °C, Cape Bird: −27.5 °C, Manuela: −26.5 °C, Eneide: −23 °C. A detailed comparison between the station data and the temperatures retrieved from AVHRR thermal imagery is beyond the scope of our study here, but we note that a one-to-one correspondence can hardly be expected for a number of reasons. Nevertheless, the station data provide an additional possibility to judge the temperature conditions in the region shown in Fig. 4. The zones of higher temperatures (yellow) delimit the range of influence from the RSP (lower right), the MSP (in a small part northwest from station Cape Bird), and the TNBP. The open water zone of the TNBP is indicated by the brownish colour. Very well reflected is also the deformation belt with smaller and larger colder (thicker) ice floes and warmer (thinner) ice between them. The dark blue area in the upper left corner of the image is a fast ice zone. The southern part of this zone is breaking off. This process manifests itself in the crack of higher temperature.

The joint analysis of optical (near-infrared), thermal, and radar imagery acquired within short time intervals (about 2 h and less) demonstrates the great advantage that multi-sensor data offer for the qualitative retrieval of ice conditions and analysis of certain processes. We regard the combination of thermal and radar data useful, since the former permit a relatively clear separation of thinner and thicker ice (with the disadvantage of being hampered by cloud cover), whereas the latter emphasize the surface roughness and narrow deformation structures. In our case, the lower frequency L-band image offers some advantages with respect to the identification of ice structures and types. However, we refrain from recommending L-band imagery for all cases. Any general (global) preference of either low- (L-band) or higher frequency radar (C- or X-band) for the discrimination of thin ice types has yet not been formulated (Dierking, 2010; Dierking and Busche, 2006). If, e.g., multi-year ice occurs in ice fields around a polynya (more frequently in the Arctic, but multi-year ice persists also in the eastern Ross Sea), C-band may be a better choice for discrimination and classification of ice types (e.g., Dierking, 2013). Optical images are useful

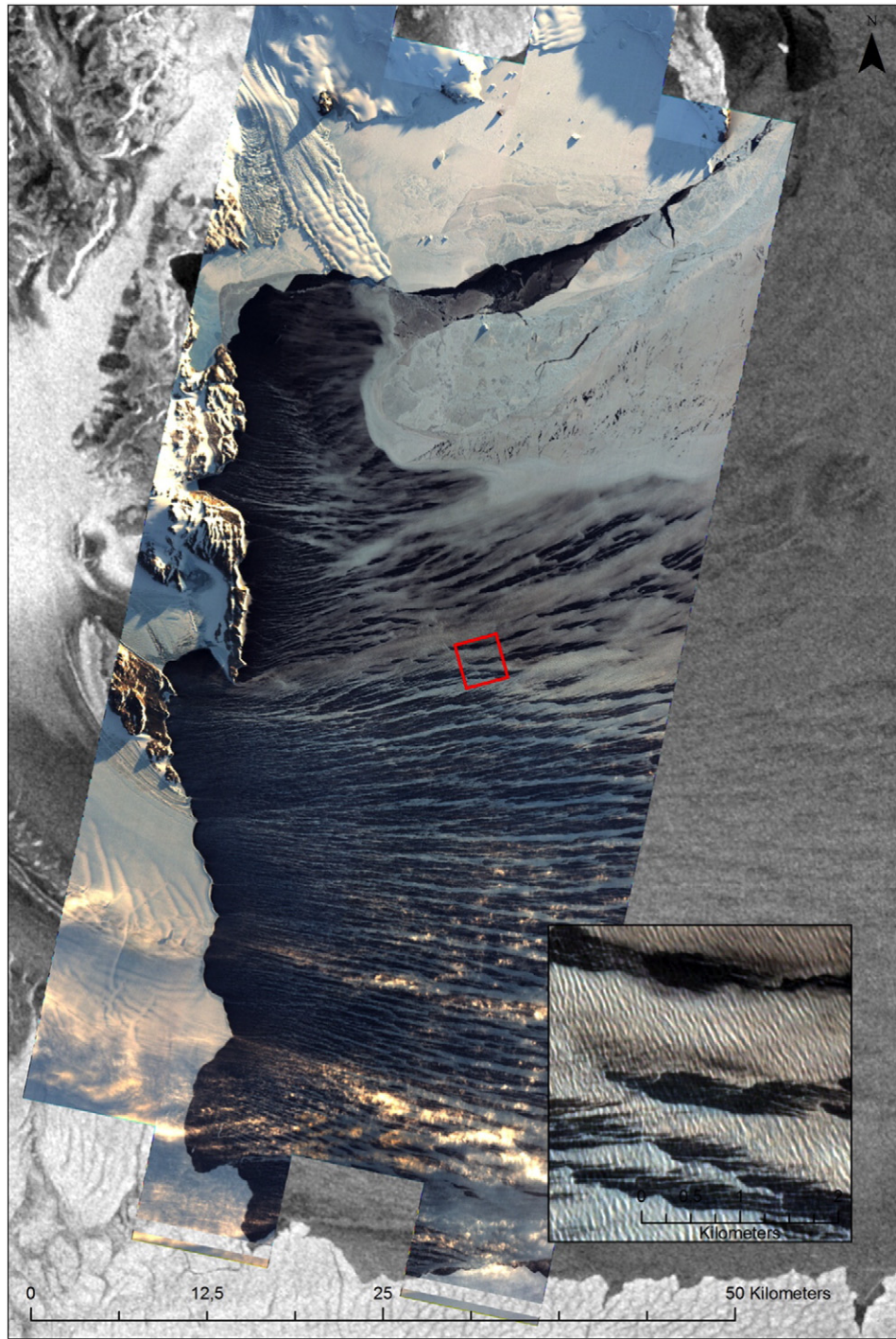


Fig. 3. EO1 ALI optical image overlaid on an Envisat ASAR WS scene. Both were acquired on Sep. 7, 2009, the former at 19:10:28 UTC, the latter at 21:19:36. The scene covers an area of about 60 km in east-west and 100 km in north-south direction. The zoom-in at the bottom (right) demonstrates that ocean waves can well be recognized in the ice streaks.

to separate snow-covered and snow-free ice, and they improve the reliability of the retrieval of ice conditions from SAR images. The example shown in Fig. 3 also demonstrates that processes shaping the ice conditions in and around polynyas (in this case the wind shaping the ice streaks) can only be fully conceived if additional meteorological and oceanographic data are available.

5.2. Regional analysis

On the regional scale, meteorological and ice conditions cause a complex interaction of the three polynyas (RSP, MBP, TNBP) in the

Ross Sea (Section 3 and Fig. 1). Fig. 5 shows an image sequence acquired with the AMSR-E from 5th to 12th of September 2009, representing the brightness temperature T_B that was measured at 89 GHz, H-polarization, and mapped with a spatial resolution of 2.2 km. One can identify the Ross Ice Shelf at the bottom of the individual images (which is in the south), and Victoria Land with the Drygalski ice tongue on the left (west). The RSP can be spotted at the right bottom, the MSP left of the bottom center, and the TNBP above (north of) the Drygalski ice tongue. In the middle of the image a bow shaped feature of lower T_B -values shows up, which separates the south-east ice cover influenced by (and partly originating from) the RSP and the north-west sea ice cover

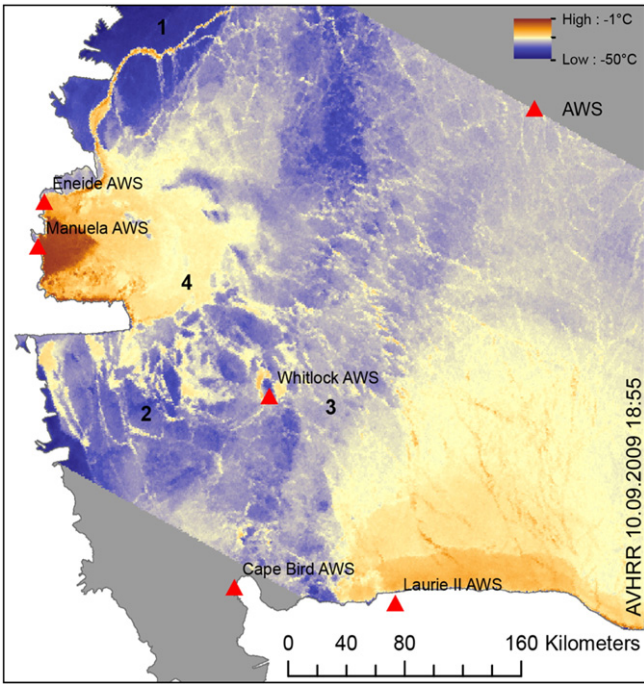


Fig. 4. Ice surface temperature derived from AVHRR 4 and 5 (11 and 12 μm). The image was acquired on Sep. 10, 2009. The spatial resolution is 1.1 km. Average surface temperatures for different ice types are: 1 fast ice (dark blue) $-40^\circ\text{C} \pm 2.9^\circ\text{C}$ 2 level ice floes (blue) $-35^\circ\text{C} \pm 1.8^\circ\text{C}$ 3 thin ice floes (light blue) $-31^\circ\text{C} \pm 1.8^\circ\text{C}$ 4 accumulation zone $-24^\circ\text{C} \pm 1.8^\circ\text{C}$ and refrozen leads (light yellow) The partially open water zone of the polynya (brown) revealed a mean temperature of -5°C .

moving away from the TNBP (see also Fig. 1). From a comparison of the AMSR-E data with the corresponding SAR images available for this period (see example shown in Fig. 6), we found that this feature corresponds to the deformation belt that is also visible in Figs. 2 and 4.

The microwave brightness temperature is the product of the emissivity ϵ and the physical temperature T of the imaged area. The emitted radiation is from the upper ice layer. Its thickness is determined by the penetration depth, which varies between a few millimeters to decimeters, dependent on ice physical properties and microwave frequency. For a frequency of 89 GHz, Mathew et al. (2008) give values of 28 cm for dry snow, 4 cm for multi-year ice, and 0.9 cm for first-year ice. The average physical temperature of the emitting layer differs from the air or surface temperature. It depends on the microphysical properties of the snow and ice and varies with microwave frequency (due to the different penetration depths). Mathew et al. (2008) determined the “emitting layer temperature” as a linear function of the air temperature for the Arctic. For first-year ice, their results reveal that the former ranges from -19°C to -8°C at 89 GHz for air temperatures between -40°C and -10°C . We assume that these results are approximately valid also for ice conditions in the Terra Nova Bay. If the ice surface temperature at two different first-year ice locations differs by 30°C , the corresponding change of T_B would hence only be about 10 K, if ϵ remains constant. The variations of the ice surface temperature T_{ice} on September 10, shown in Figs. 2 and 4 for the Terra Nova Bay, range from approximately -45°C to -15°C (-2 to -4°C in the polynya zone of partially open water, see Fig. 7 below). The brightness temperatures T_B in the corresponding area are between approximately 195 K and 235 K. The polynya zone is not recognizable in the microwave image, which we attribute to the coarse resolution and the mixed-pixel effect. Considering that the range of the emitting layer temperature is smaller than the one of the ice surface, the variations of T_B must also be influenced by the emissivity. The emissivity ϵ of ice depends on the ice temperature, surface roughness, porosity, snow wetness, snow grain size, ice layers in the snow, presence of slush or superimposed ice on the

surface, and in the case of sea ice on salinity, brine volume fraction, brine pocket shape and spatial distribution (Shokr and Sinha, 2015). At 90 GHz, ϵ of open water is 0.528, for new ice 0.573, and for first-year ice 0.886 (Shokr and Sinha, 2015, Table 8.10). Their Fig. 8.32 shows that ϵ increases significantly during the first 10 mm growth of ice, but then reaching values typical for first-year ice. Hence, we expect larger variations of ϵ only in areas of open water, grease and thin ice, e.g., in the outlet zone and in leads. Fig. 7 shows a graph relating T_{ice} and T_B , which reveals slightly growing T_B -values with increasing T_{ice} for the zones of fast ice, smooth ice floes, and rough floes (blue in Fig. 4). For the zones of accumulated ice (yellow and orange in Fig. 4), a clear relationship between T_{ice} and T_B was not found: the interval of T_{ice} is mainly clustered between -20°C and -27°C , the corresponding range of T_B from 218 K to 239 K, which results in a range of ϵ between 0.86 and 0.97, typical for first-year ice of varying roughness (see Shokr and Sinha, 2015, Fig. 8.37 demonstrating the effect of surface roughness). The highest values of T_{ice} (-4 to -5°C) are from the frazil ice and open water zone of the polynya, in which T_B varies between 200 and 220 K. Here, we did not correct for the emitting layer thickness. The result indicates the presence of rafted and broken ice. For the fast ice, level ice, and thin ice floes (bluish colors in Fig. 4) we also obtain emissivities of first-year ice thicker than a few centimeters.

The warmer outlet zones of the RSP and the TNBP in Fig. 5 (covering the open water zone and the polynya ice pushed offshore) are characterized by spatial brightness temperature variations between 215 K and 235 K on Sep. 10 (the date is selected with reference to Fig. 4). The colder deformation belt reveals variations of T_B between 195 K and 215 K (blue-yellow) with interspersed warmer (thinner) ice (orange) over the period from Sep. 5 to 12. On Sep. 12, however, it decreased in width. The deformation belt as a zone of shear between the southeast RSP ice and the northwest TNBP ice can be identified over the whole image sequence shown in Fig. 5. Its contrast in brightness temperature may be related to the magnitude of the forces exerted on it, which causes stronger ice deformation. Unfortunately, we do not have the necessary data (ice and wind conditions, ocean currents) to prove this hypothesis.

The T_B -pattern observed in the AMSR-E 89 GHz data can also be recognized in the 36 GHz channel, although the signature contrast is less. This may be caused by the lower spatial resolution of the 36 GHz channel. The deformation belt can be observed regularly over the years.

6. Separation of ice zones

In this section we deal with the segmentation and classification of distinct ice zones in the Terra Nova Bay. In and around a polynya different stages of new ice formation are found, e.g., accumulations of frazil and grease ice due to compressional forces exerted by the katabatic wind, and consolidated thin level ice that may reveal deformation structures (rafting, ridging). In our study, the aim of segmentation and classification (the latter is linking segments and actual ice conditions) must be to reconstruct different steps in the evolution of a polynya. The individual ice zones may have completely different properties regarding salt release, heat exchange, and deformation. For an example of classification we combine the near-simultaneous multi-sensor satellite acquisitions over the TNBP shown in Fig. 2, which have comparable spatial resolutions (here, we do not consider the coarse-resolution PMR data).

In a first step, we looked at the segmentation potential of different sets of discrimination rules (supervised hierarchical approach) and of unsupervised clustering algorithms (such as ISODATA). In both cases, spatially varying mean values and variances of the directly measured quantities (reflectance, temperature, backscattering coefficient) are determined. After dividing the images into different segments, they have to be linked with actual ice classes in a second step. For supervised classifications an operator identifies areas of interest in training data that mirror the statistical characteristics of single isolated ice zones. Several

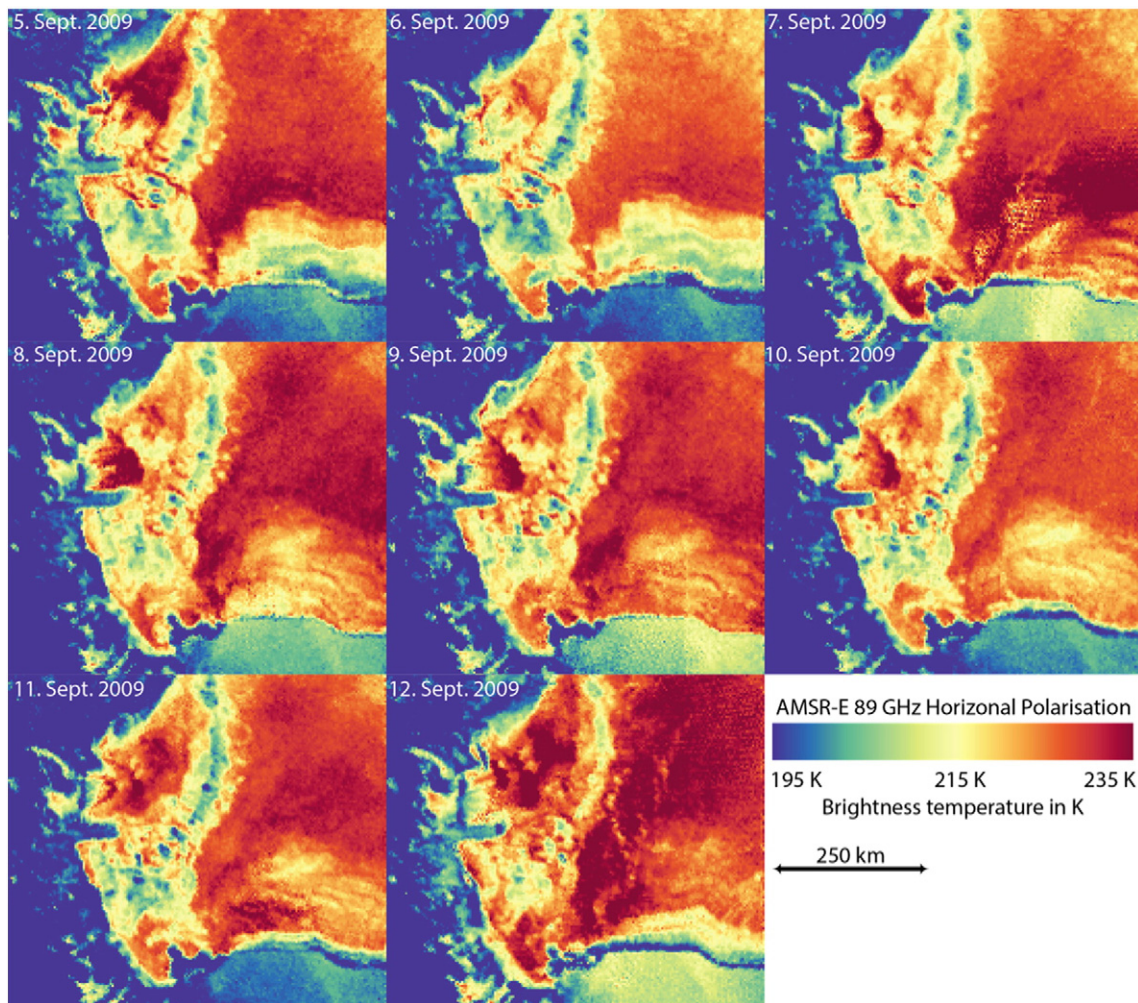


Fig. 5. Sequence of images from AMSR-E 89 GHz, H-polarisation, for the period from Sep. 5 to 12, showing the brightness temperatures TB at an enhanced resolution of 2.2 km. Blue colors indicate lower values of TB, red colors higher values.

approaches are available, spanning the range from various distance measures that are used to associate each pixel with a certain segment, to highly complex systems such as neural networks or supported vector machines. The manual identification of training classes is time consuming and ambiguous (due to the subjective component of human interference). An alternative is the use of unsupervised techniques. A popular approach in this group is the ISODATA algorithm. Such approaches can handle multidimensional data and classify multi-sensor data. The advantage is that they often detect segments that might be difficult to recognize by visual analysis. While visual separation of segments is still possible when combining data of two or three different channels, sensor modes, or sensors, it becomes impossible in four or more dimensions. The disadvantage of unsupervised methods is that their results are often difficult to link to a classification scheme that is optimally adapted to the actual (ice) conditions. For our ISODATA classification we found that a supervised post-adjustment was necessary to adapt the automated segmentation to the actually present ice conditions, which devalues the advantage of unsupervised techniques. In this section, we focus therefore exclusively on the supervised segmentation. Land and cloud-covered areas are excluded from the classification procedure.

Since the MODIS NIR reflectance image (Fig. 2) is more difficult to interpret than the thermal AATSR data and more severely affected by clouds, we decided to include only the latter into a segmentation scheme, together with the C- and L-band radar images. While C-band

allows a good differentiation of the different ice types and floes, L-band reveals a stronger backscatter for highly deformed regions (e.g. deformed polynya ice or deformations such as rafting and ridges). SAR images acquired under freezing conditions show many more details about ice structure (floes, cracks, brash ice etc) than optical and thermal sensors, because the radar signals penetrate through dry snow. The thermal sensor eases the separation of open water, thin and thick ice without being hampered by too many small structural details.

The ideal classification in the area of TNBP should comprise the following elements.

1. The pack ice zone consists of differently sized thicker ice floes with interspersed thin ice. Thicker ice floes reveal lower surface temperatures and moderate to high backscattering intensity due to different stages of deformation and fracturing. Thin ice manifests itself through higher temperatures and lower backscattering coefficients.
2. The outlet ice reveals a sequence with alternating accumulated, partly banded ice and broken ice floes that partly reveal signs of ridging and rafting. The surface temperature is high and does not show any differences between accumulated ice and ice floe zones. It gradually decreases with distance from the polynya. The backscatter intensity is high over accumulated ice (indicating a rough surface) and lower over the ice floe zones.
3. The open water polynya zone can be easily recognized because of its very high temperature. The backscattered intensity depends on the

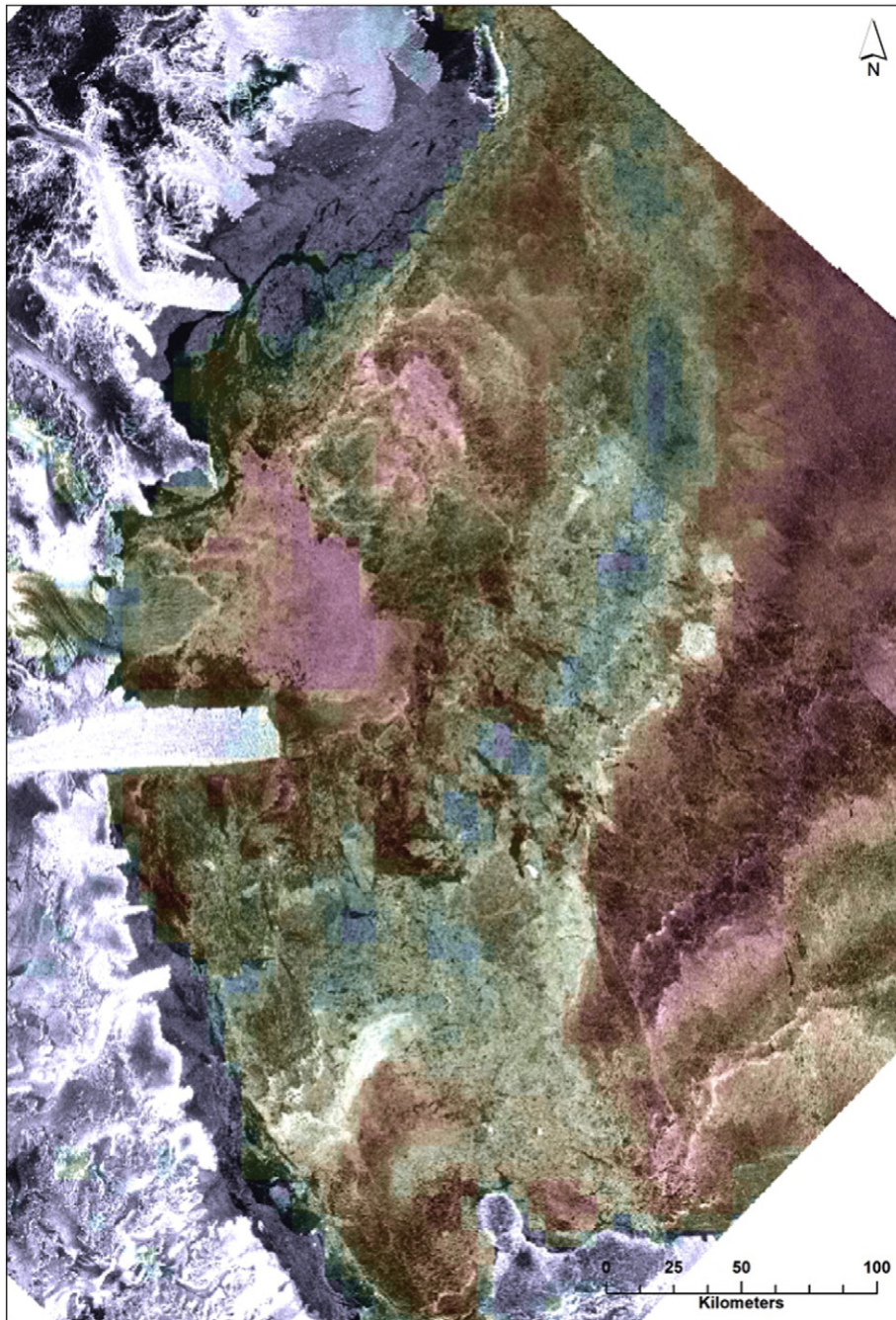


Fig. 6. Brightness temperature TB measured on September 10, superimposed on a mosaic of the ASAR and PALSAR images acquired on the same day. The magnitude of TB decreases over the deformation belt (recognizable as bluish colour).

- radar frequency. For each frequency band it is highly variable, since it is influenced by wind speed and direction, as well as by the presence and areal density of streaks of frazil ice.
4. Fast ice is characterized by low temperatures and relatively low backscattering intensities. It forms partly rather homogenous areas with weak indications of surface structures. We also found areas of apparently former fast ice, which broke off and started to drift.
 5. Land ice reveals very low temperatures and high backscatter both at L- and C- band.

Our *hierarchical segmentation* approach considers the five general classes described above and is formally constructed as a *decision tree* shown in Fig. 8, which sorts the individual pixels according to their respective values (magnitude of the measured quantity) in the images

used for classification. The ice zones were selected such that special aspects of the ice conditions important for our analysis are emphasized, e.g., the deformation belt and the outlet zone. The segmentation is started with the determination of suitable threshold values between the ice zones and types listed above. To this end we used plots of histograms showing the distributions of the measured backscattering coefficient or temperature for each ice type (not shown). The decision tree in Fig. 8 starts with separating land (as very cold) and the open water/partially open water zone of the polynya (as warmest area), as described in items 3 and 5 of the list of classification elements above. Besides the AATSR surface temperature, the L- and C-band backscattering intensities are needed for minimizing the level of ambiguity in identification both classes. The temperature difference between thinner and thicker ice is then the major criterion for distinguishing the outlet zone from

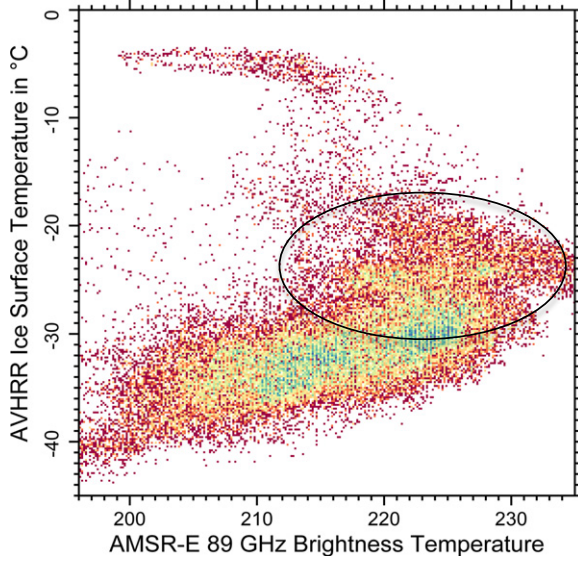


Fig. 7. Comparison of brightness temperature from AMSR-E 89 GHz (H-polarization) and sea ice surface temperature derived from AVHRR data. The colors indicate the frequency of the respective combinations of surface and brightness temperatures (increasing from red to blue). The ellipse indicates values obtained from the accumulation zones.

the deformation belt and adjacent pack ice (items 1 and 2 in the list above). The decision tree ramifies into a “pack ice” branch (bluish and greenish colors) and a “thin/outlet ice” branch (red and violet colors). For each branch, the surface characteristics are retrieved from the radar images. L-band is well suited to split off the high intensity regions, i.e. accumulated ice in the outlet zone, and the floes of consolidated ice

in the pack ice and deformation belt zones. Finally, C-band is used to distinguish different stages of surface roughness in both cases. With “rough” ice we refer to surfaces with small-scale height variations of the order of millimetre to decimetre (including, e.g., brash ice). The notation “deformed ice” points to the presence of structures such as single or groups of ridges or rubble fields. We are constrained to this “radar-view” classification because we do not have high-resolution optical images available over most parts of the scene. Fast ice (item 4) appears in the pack-ice branch of the decision tree, mainly as consolidated and smooth ice.

The decision rules were then applied pixel-by-pixel to the AATSR, L-, and C-band SAR images (with the AATSR being re-sampled to 100 m pixel size). The result is depicted in Fig. 9. Here, the extension of the outlet zone is clearly visible. In the deformation belt, a relatively high fraction of thinner ice is found (such “warm” areas are also interspersed in the brightness temperatures observed over the deformation belt in Fig. 5). Possible manifestations of ice formed in the MSP and the RSP can be recognized at the bottom and the right margin of Fig. 9. The advantage of such classification maps for polynya research is that the extent of different polynya zones can be quantitatively determined, and variations of ice characteristics due to formation under calm conditions or strong katabatic wind events can be well separated. The segmentation procedure sketched here was optimized for the data set we had available, and for the conditions that are specific to the ice conditions in and around Terra Nova Bay. In Section 8, we address more general aspects.

7. Ice drift field

Ice drift and deformation are among the essential parameters for polynya observations, as mentioned in Section 2.4 above, in which also the basic principle of ice drift retrieval is briefly sketched. The most eye-catching characteristics of an evolving polynya are its fast spatial and temporal changes. The motion patterns of the ice around polynyas can

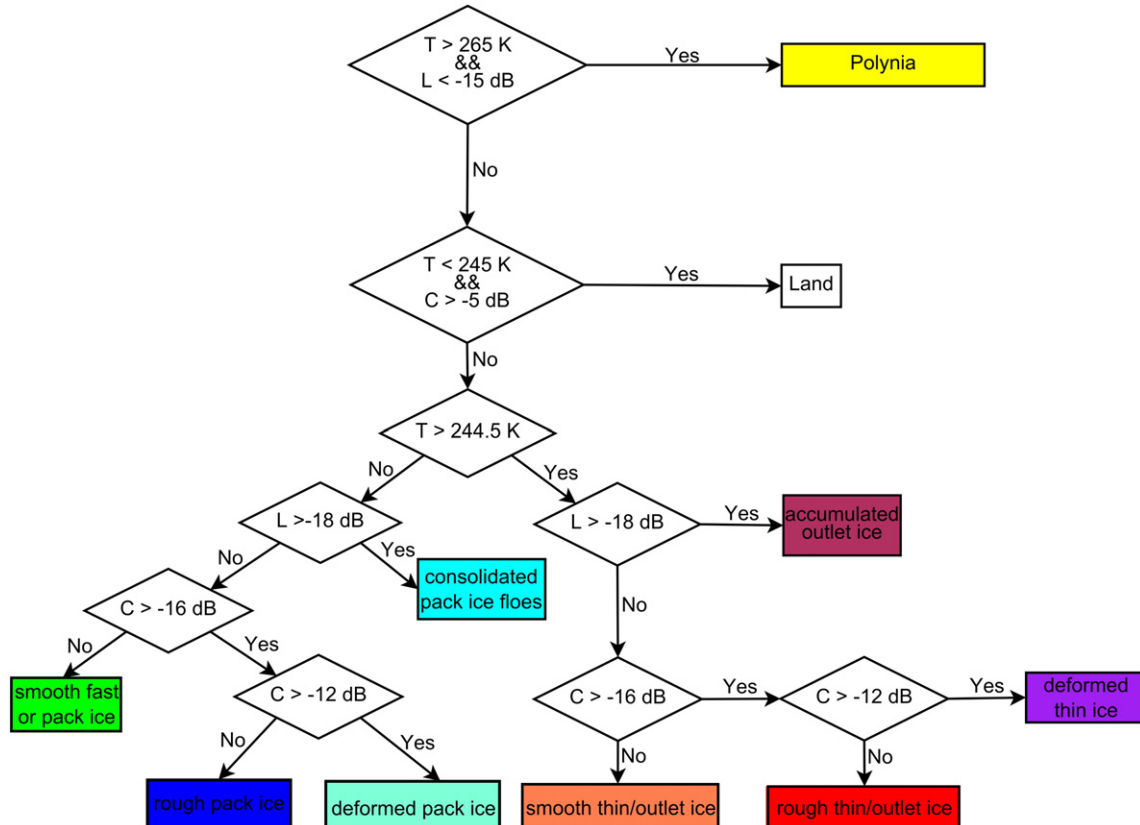


Fig. 8. Decision rules for separating different ice zones. For further explanations see text.

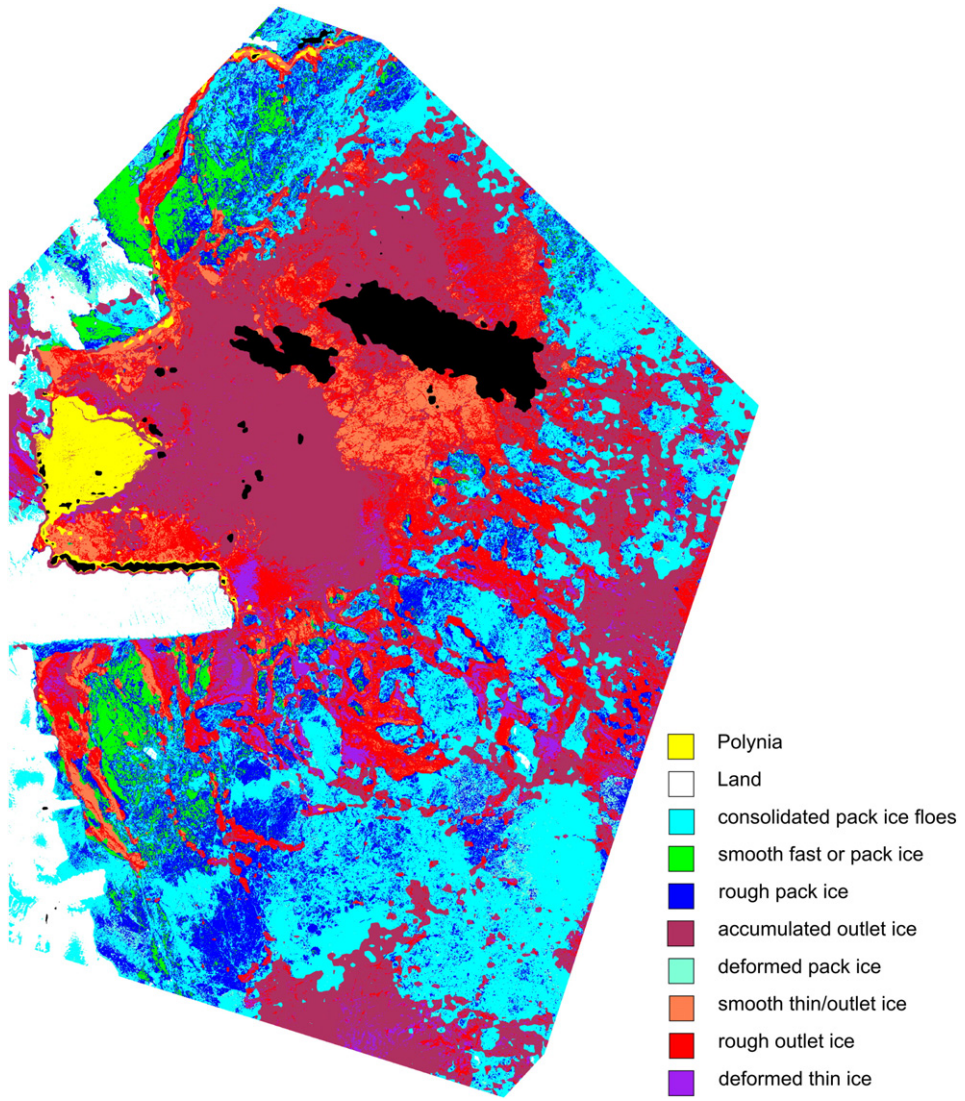


Fig. 9. Result of the classification. The colour scheme corresponds to the decision tree of Fig. 8. The black areas correspond to the locations of clouds.

be derived from sequences of satellite SAR images that are acquired with temporal gaps of a few hours to a few days. Since the ice cover in a polynya may change within minutes (frazil streaks) to hours (accumulated or loosely consolidated, banded ice), the frequency of recent operational satellite SAR image acquisitions is usually too low. Together with the segmentation and classification approach, the motion field provides information on the temporal variability of the different ice zones, the degree of deformation, and the export of ice away from the region.

Fig. 10 shows the drift fields obtained for the ASAR image pairs 6–7.9., 7.–9.9. and 9.–10.9.2009. The drift from 10.–11.09.2009 was retrieved from ALOS PALSAR images. As background for the figures, the first image of each pair is used. The retrieved drift fields passed the reliability check of our algorithm (Hollands et al., 2015), which indicated the existence of mostly stable image patterns suitable for ice motion tracking. The area over which the drift patterns can be retrieved depends on the spatial overlap between images 1 and 2, which explains the different coverage of the drift maps shown in Fig. 10. The sequence of drift maps reveals strong northeast movements of the ice outlet in the first and the last image pair, and very small displacements between Sep. 7 and 10. From Sep. 7 to 9, the movement is mostly to the east, and from Sep. 9 to 10 to the north and northwest. Results in the immediate polynya area are less reliable, since the corresponding image patterns change very fast. When forming an image pair using the SAR acquisitions from

Sep. 7 and 10 (Fig. 11), the spatial overlap is at maximum and reveals also the drift pattern southeast of the ice outlet and the adjacent deformation belt (although variations of the motion paths taking place on temporal scales lower than 3 days are lost). In the area south of the Drygalski ice tongue, the ice is first pushed to the west (right side), then, because of the adjacent coast, to north-northwest (beneath the ice tongue), and finally turning to northeast. More to the east (right side of the image), the drift direction is north-northeast. This is in agreement with the results of model simulations presented by Gallée (1997), his Fig. 5). The large-scale average ice motion in the south-west edge of the Ross Sea (obtained from passive microwave radiometer data over a period of 17 years from 1992 to 2008) for the month September is mainly northward (Comiso et al., 2011, their Fig. 9).

Fig. 12 depicts the wind speed magnitude in our observation period. The wind speed increased in the afternoon of September 6 and decreased subsequently in the late evening of the next day. Another high wind speed event took place on September 11 and 12. In both cases, the ice outlet movement was significant, although slightly less strong at the second occasion.

The segmentation map (Fig. 9) provides a snapshot of the ice conditions at a particular time, hence a “static” view. The corresponding “dynamic” information is provided by a drift (or displacement) map, obtained by adding a second image acquired earlier or later, with the shortest possible temporal difference. Fig. 13 shows the example

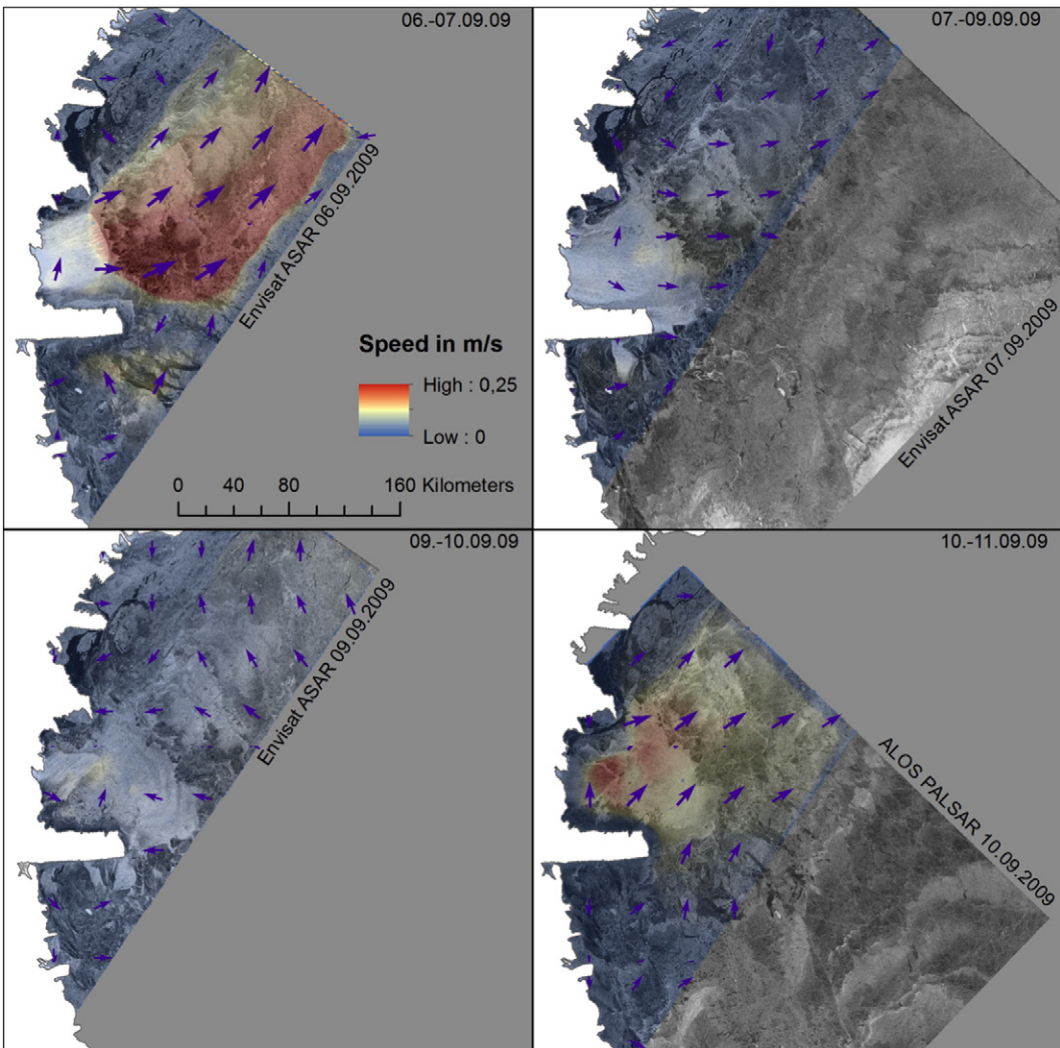


Fig. 10. Sea ice drift derived from different ASAR image pairs and one PALSAR pair (bottom right). Colour zones represent different drift velocity intervals, arrows (scaled to velocity) show dominant local drift direction.

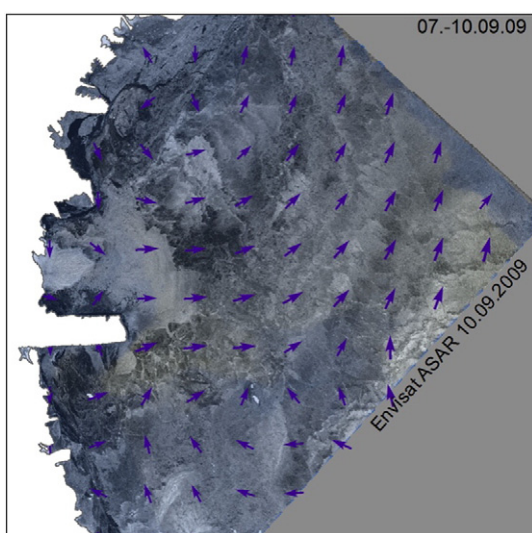


Fig. 11. Motion patterns retrieved from two ASAR images acquired with a 3 days temporal gap. The overlap zone between images 1 and 2 is here at a maximum (compare to Fig. 10).

corresponding to the segmentation map of Fig. 9. The accumulation zone in the polynya outlet reveals a higher velocity (0.16 m/s, about 0.5 km/h) than the larger and more stable ice floes at its end in the northeast (brown area and part of the light green zone in Fig. 13, with 12–10 m/s), which explains its strong deformation (i.e. generation of a rough surface due to accumulation of grease ice, and rafting and break-ups of the consolidated ice). In the deformation belt south of it, the velocity increases at larger distances from the coast, which is an agreement with the relatively large fraction of warm, thin ice between the colder, thicker ice floes in the segmentation map Fig. 9. The analysis of the changing drift field (the dynamic polynya regime) is needed for studying the influence of the katabatic winds on the ice offshore of the open water zone of the polynya. With a sufficient spatial coverage, it is even possible to analyse the interaction between the outlet zones (or “ice drainage areas”) of the RSP, MSP, and TNBP.

8. Discussion

One major question to be addressed in this discussion is concerning the gain that is achieved by combining various sensor data for the retrieval of different parameters which are required for understanding and modelling the evolution of a polynya (see Section 2). In the following discussion of our results (Sections 5–7) we refer also to Section 3

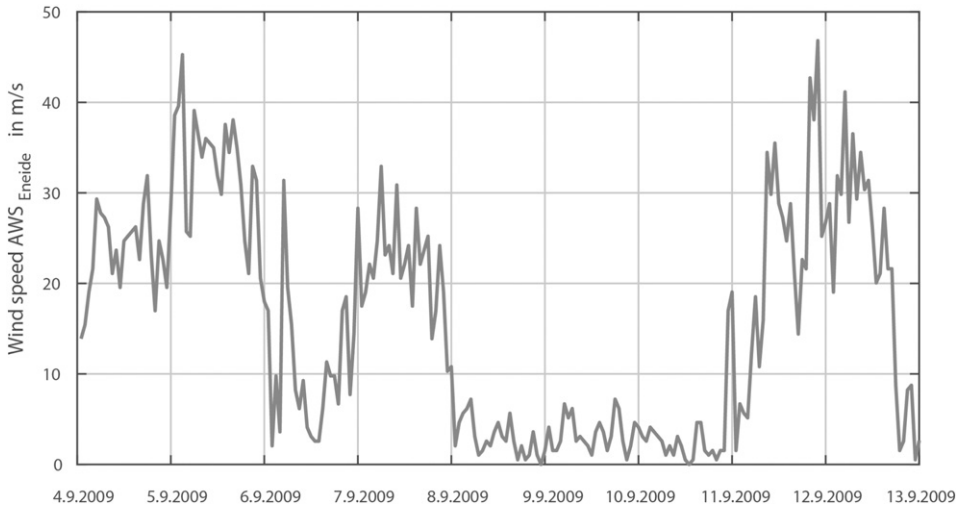


Fig. 12. Wind speed at the automated weather station Eneide.

and analyse the potential of multi-sensor data with regard to the retrieval of different polynya parameters.

8.1. Polynya zones

The cases that we could analyse with the available data revealed that optical images with spatial resolutions of 10–30 m and SAR images with

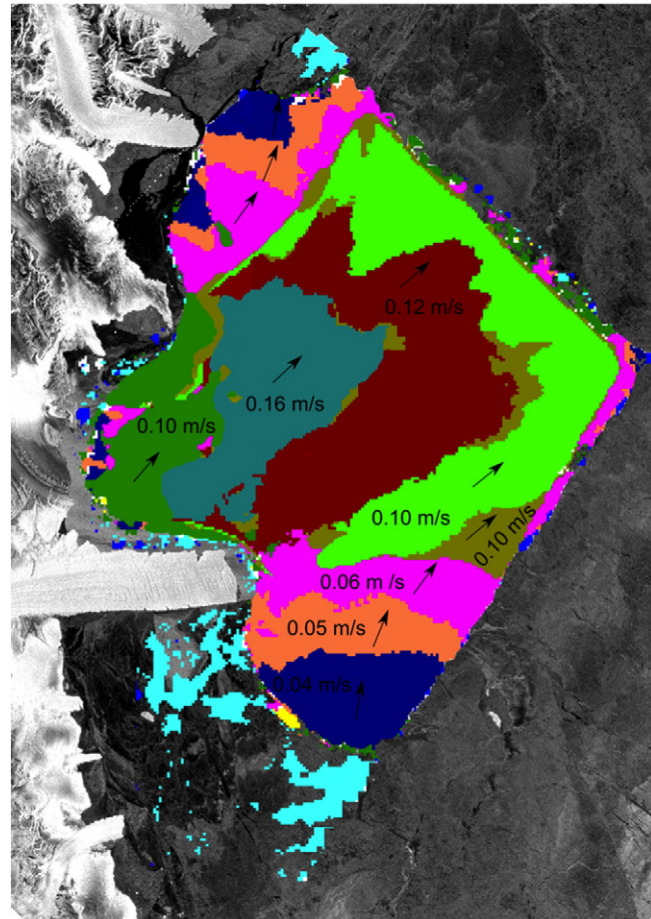


Fig. 13. Segmentation of ice drift zones for the image pair 10–11.9. Segments were separated according to their average drift speed. Arrows indicate main drift direction of each cell. Patch-like structures at the margins are edge effects. The reliability of the drift retrieval in the open-water area of the polynya is low.

resolutions of 100–150 m (Figs. 2 and 3) are well suited to distinguish different zones of the ice region influenced by the dynamics of a polynya. With reference to the definitions of different polynya widths by Williams et al. (2007) (Section 2.1), we could visually easily separate the zones of open water and partially open water, the latter being an area covered with streaks of frazil and grease ice. However, the “practical width”, which is the ice area too thin for safe travel, cannot be defined from remote sensing data, since the notation “safe travel” was not linked to any specifications of ice thickness by Williams et al. (2007). The “full width” is the extent of ice that is thinner than the adjacent pack ice. In optical, thermal and radar images, ice formed in the polynya eventually reaches a stage of development at which it cannot be distinguished anymore from offshore pack ice. The problem to determine the transition from “polynya ice” to “pack ice” is hence very difficult.

In the SAR images of the TNBP, we recognized a zone of alternating rough, “banded” areas of accumulated ice formed during periods of strong katabatic winds and relatively smooth ice floes grown under calm conditions. The ice in this outlet zone moves in northeast direction, bounded by shear zones. It is part of the total export of ice produced by the RSP, MSP, and TNBP, which varies with season and from year to year (see, e.g., Comiso et al., 2011; Tamura et al., 2008). It is hence difficult to define the full polynya width according to Williams et al. (2007). One possibility is to limit the extent to the outward edge of the first zone of accumulated, banded ice, which is easy to recognize in SAR images because of its high radar backscattering intensity. An alternative option is to rely on the ice surface temperature (Fig. 4) and limit the polynya extent by a temperature value that corresponds to a threshold for a specific ice thickness (e.g., 0.2 or 0.5 m, see Subsection 8.2). This, however, requires the consideration of atmospheric radiation fluxes and turbulent fluxes of heat (Preußer et al., 2015), which vary dependent on meteorological conditions. The first option is more meaningful, since the ice surface temperature does not allow the identification of different ice zones linked to the temporal sequence of polynya events (opening and closing) as do the SAR images.

8.2. Polynya shape

Since the coastline, and the boundaries of the open water area can usually very well be recognized in SAR images, such images are also optimal to determine the polynya and coastline shape (see Section 2.2). As Darby et al. (1995) point out, the edge of the TNBP might approximately follow the L-shaped coastal segment formed by the northern side of the Drygalski ice tongue and the margin of the Nansen ice sheet. According to Darby, the occurrence of such situations depends

on the drift direction of frazil ice in the polynya and of the pack ice adjacent to the polynya. Our analysis in [Section 5](#) revealed that such a model is too simplistic, since it does not consider the existence of the outlet zone as transition between the polynya area (consisting of open water and streaks of frazil ice) and the pack ice in the deformation belt and east of it. A more advanced approach has to take into account blocking effects between the different ice zones, which manifest themselves in differences of their drift velocities and directions.

8.3. Ice production rate

The estimation of ice production rate in polynyas, requiring the determination of the polynya area and (thin) ice thickness, is challenging as noted in [Section 2.3](#). The method that is usually applied (e.g., [Tamura et al., 2008](#); [Willmes et al., 2010](#); [Preußner et al., 2015](#)) is based on the estimation of the local heat budget (assuming that the entire heat loss contributes to the formation of new ice), and is only applicable over areas of undeformed thin ice <0.5 m in thickness, in some studies even restricted to values <0.2 m. The surface temperature of very thin snow-free ice is close to the freezing point of the upper ocean layer ([Preußner et al., 2015](#)). Dependent on its relative contribution to ice production, also the frazil ice growth in the open water area needs to be considered (e.g., [Jardon et al., 2014](#)). In our case study, the open water zone and the adjacent ice area can be well separated in the AATSR TIR image ([Fig. 2](#)) but the temperature does not reveal any clear difference between the alternating areas of accumulated, rough ice and distinct ice floes in the outlet zone. (Note that we attribute the variations close to Drygalski tongue to small clouds.) The surface temperature decreases at larger distances from the polynya, which we interpret as increasing ice thickness. The equations for retrieving ice thickness h_t and calculating ice production rate dh_t/dt require the conductive heat flux through the ice and the ice density as input parameters. The former depends on density, temperature, and salinity of the ice ([Pringle et al., 2007](#)). Most presumably, the differences of density and conductivity between the areas of accumulated ice and distinct ice floes in the outlet zone (as clearly recognizable in the SAR images) are not negligible, and in particular the accumulated ice areas may violate the basic assumptions (presence of consolidated smooth level ice, linear temperature profile) of the method for ice production estimation. If available, high-resolution optical data such as from the EO-1 ALI ([Fig. 3](#)) may provide even more detailed information about ice zone characteristics.

SAR data may be usable to estimate the thickness of thin sea ice. One method, e.g., is based on the observation that thickness and the co-polarization ratio (between radar intensities at VV- and HH-polarization) are correlated ([Wakabayashi et al., 2004](#); [Nakamura et al., 2009](#); [Toyota et al., 2009](#)). This can be attributed to the fact that the co-polarization ratio is sensitive to the dielectric constant, which changes due to desalination of the ice during ice growth. Since such methods are based on empirical equations, which are derived for specific ice conditions, they must be adapted to polynya areas. In summary, the analysis of high-resolution (150 m and better) SAR and optical imagery deliver a more detailed picture of the often highly variable ice conditions in areas for which ice production rates shall be calculated. A more detailed investigation of how high-resolution imagery can be utilized to develop more accurate methods for ice production estimation is beyond the scope of this study. It is, however, obvious, that the ice thickness retrieval based on SAR imagery is an important topic in this context.

8.4. Ice drift and deformation

Another issue is concerned with the retrieval of ice drift and deformation. Limitations of the retrieval, e.g., due to the relatively coarse temporal resolution in acquisitions of high spatial resolution satellite images, are mentioned in [Section 2.4](#), and its advantage for the separation of dynamic regimes is discussed in [Section 7](#). Ice deformation needs to be considered in the retrieval of ice thickness (see above) and in

model simulations of polynya dynamics. In high-resolution SAR images (and also in optical imagery under favourite light conditions), single rafting zones, ridges, Langmuir cells, and banding structures parallel to the coastline can often clearly be separated from smooth level ice. Besides spatial resolution, their perceptibility depends on radar frequency, polarization, and incidence angle. [Dierking and Dall \(2007\)](#), e.g., found that ridges and rafting zones are easier to recognize using lower frequencies (L-band) and/or cross-polarization (HV,VH). Zones of new ice reveal much larger signature variations at higher radar frequencies (e.g., [Dierking and Busche, 2006](#), their [Fig. 3](#)). Those results were obtained for freezing conditions. When the ice surface is covered by moist snow, the separation of ice classes can be easier at L-band, since longer radar waves penetrate deeper into the snow and ice (e.g., [Casey et al., 2016](#)). Nevertheless, the major parameter for the analysis of detailed spatial variations is the corresponding resolution. For the detection of ridges and rafting, [Dierking and Dall \(2008\)](#) recommend resolutions better than 5 m.

8.5. Polynya ice classification

In [Sections 6 and 7](#) we use a segmentation approach for separating different units of the ice cover and zones of different ice drift. We regard the latter important to consider adequately the dynamic nature of a polynya. Segmentation algorithms allow the separation of location and areal extension of different ice zones. Such algorithms are based on image signature variations, which are caused by the changes of the measured quantities. Signature variations, however, are not necessarily always directly related to different ice classes. E.g., variations of the centimetre-scale surface roughness on one ice floe may significantly change the backscattered radar intensity.

For the work described in [Section 6](#) we carried out a test with an unsupervised algorithm. The test revealed that it is difficult to relate the automatically determined segments to the relevant ice types and conditions in and around the TNBP. Since a manual post-processing is required also for the unsupervised segmentation, it may be more efficient to develop a supervised procedure from the beginning. A method such as the decision tree described in [Section 6](#) offers the flexibility to consider the knowledge about specific ice conditions, the respective information content in the data products from different sensor types, and the scientific question to be addressed. A flexible segmentation scheme allows the integration of data from various sensor types based on availability. Another advantage is that input data can be weighted differently. It is, e.g., possible to use weather independent SAR data as main source and include the cloud-influenced thermal infrared data only if needed for additional decision rules or for enhancing the robustness of certain rules. A problem, however, is that such segmentation schemes cannot be applied globally. The adaption to local ice conditions at different polynya sites is required (including the final classification, i. e. linking of ice types and conditions to the different segments). Even a scheme developed for a specific polynya site needs to be changed as a function of time, considering temporal and seasonal changes of ice conditions and melting events. In general, the more detailed the classification scheme is, the more detailed it needs to be adjusted to the actual ice and environmental conditions. Another problem is the validation of classification results since usually, the necessary ground data are not available. The principally achievable sea ice classification accuracy based on Sentinel-1 images, e.g., is discussed in [Torres et al. \(2012\)](#). The issues of changing conditions and achievable classification accuracies require further studies.

8.6. Choice of satellite instruments

The selection of specific satellite sensors for polynya research depends on the scientific objectives, as studies mentioned in the introduction and in [Section 2](#), as well as our own work demonstrated. This concerns in particular the proper choice of spatial and temporal

resolution and coverage. In Table 3, instruments are listed that are most suited for the retrieval of the polynya parameters mentioned in Section 2. Typical ranges for resolution and coverage are given in columns 2 and 3. The use of coarse-resolution large-coverage sensors such as thermal IR and passive microwave radiometers or optical imagers is of advantage if very large polynyas such as the RSP or larger regions with several polynyas shall be investigated with a high temporal resolution (Section 5.2). If single polynya zones and ice types and structures need to be discerned, sensors with moderate to very high spatial resolution (100 m–1 m) are available (Section 5.1). Pros and cons of different instruments are discussed in Section 2. The retrieval of thin ice thickness by SAR (listed for the estimation of ice production rate in Table 3) is not mature yet but may become an important tool in the near future. In case of optical images it is unknown whether the ice below the snow is thin or thick. In the thickness retrieval using thermal IR measurements, the influence of snow on the measured ice surface temperature has to be considered explicitly. If the snow is dry, its effect on radar signatures can be neglected in many cases.

8.7. Coordination of measurements

An important point is the coordination of satellite data acquisitions over polynya regions, in particular, if satellites do not continuously image the Earth's surface or have to be switched between different imaging modes, and if they are operated by different space agencies. Up to date, e.g., a central tool for providing location and time of future data acquisitions of all Earth Observation satellites is still missing. A more coordinated acquisition of multiple sensor satellite data for polynya research is essential in conjunction with field measurements of complementary meteorological and environmental data. Automated weather stations, however, are sparse in the Antarctic. Polynya research in general and the utilization of remote sensing technologies in particular would greatly benefit from field and airborne campaigns, that focus on the co-incident collection of atmospheric, oceanographic and sea ice data to improve and/or validate the methods for retrieving polynya properties.

9. Conclusions

The goal of this study was to demonstrate the potential of multi-source satellite data analysis in conjunction with investigations of polynya dynamics. We focussed our study on the frequently occurring

Terra Nova Bay Polynya in the Ross Sea, which can well be covered by wide-swath SAR imagery. Besides SAR data acquired at C- and L-band, we had near and thermal infrared, visible, and brightness temperature data available. The highest spatial resolution was 10 m (EO1-ALI panchromatic mode), the coarsest 2.2 km (AMSR-E, enhanced).

In thermal and SAR images we could identify the outlet zone in which the ice formed in the polynya is pushed offshore between the pack ice. The outlet zone consists of rougher accumulation ice that develops at conditions of stronger katabatic winds and alternates with areas of distinct ice floes indicative of calm conditions. We suggested to determine the polynya width as the distance from the coast to the offshore margin of the first accumulation zone since this can be clearly identified in radar images. By comparing AMSR-E and SAR images we found that a belt of deformed ice (thicker ice floes with thin ice between them) can be well recognized in the former over longer time periods. This belt comes into being because of the strain exerted by northward ice movements triggered by the McMurdo Sound Polynya and the Ross Sea Polynya and the eastward ice export in the Terra Nova Bay Polynya outlet zone. The existence of streaks of frazil and grease ice in the open water area of the Terra Nova Bay Polynya was documented in high-resolution optical images. The streaks could also be found in the SAR images, but their identification was more difficult because of weak signature contrast and a low ratio of feature dimension divided by image resolution.

A decision tree was constructed for image segmentation, based on SAR and thermal data. The inclusion of thermal infrared imagery into the decision process turned out to be highly valuable in the polynya ice regime. The resulting segmentation map can be used to separate different stages of ice and to determine quantitatively the extent of different regions such as the polynya outlet zone and the deformation belt occurring east of Terra Nova Bay. We recommended the application of supervised segmentation schemes that can be adapted to the specific ice conditions and sensor data, considering the major scientific question. If a second image is available that was shortly taken before or after the radar image used for segmentation, it is possible to retrieve drift and deformation patterns in the polynya ice regime. The “static” classification of momentary ice stages can thus favourably be supplemented by delimiting different “dynamic” zones in the polynya ice regime.

The investigations reported in this paper were motivated by the fact that the Sentinel satellite missions of the European Space Agency offer

Table 3
Choice of satellite sensors for the retrieval of polynya parameters.

Polynya parameters	Sensor	Coverage	Spatial resolution	Specific purpose
Area and extent	Imager/scanner (VIS, NIR, TIR)	30–200 km	10–60 m	+ separation of polynya zones and boundary: open water, open water with streaks of frazil/grease ice, accumulation belt, thin ice, pack ice;
	SAR	15–500 km	3–100 m	+ determination of polynya shape + detection of polynyas, + estimation of polynya sizes, + monitoring of temporal evolution
	Imager/scanner (VIS, NIR, TIR)	>2000 km	250–1000 m	+ optical data: snow cover + TIR: thin and thick ice separation
Ice types	Passive microwave radiometers	1500 km	>5 km	+ SAR: ice age, ice structure
	imager/scanner (VIS, NIR, TIR)	30–200 km	10–60 m	+ local drift and deformation in a polynya region
ice drift	SAR	15–500 km	3–100 m	+ detection of thin ice, rafting, and frazil/grease ice streaks
	SAR	400–500 km	100 m	+ thin ice thickness retrieval
ice production	Imager/scanner (VIS, NIR, TIR)	30–200 km	10–60 m	+ thin ice thickness retrieval
	SAR	15–500 km	3–100 m	+ thin ice thickness retrieval
	Imager/scanner (VIS, NIR, TIR)	>2000 km	250–1000 m	+ thin ice thickness retrieval
regional characteristics	passive microwave radiometers	1500 km	>5 km	+ thin and thick ice distribution
	Imager/scanner (VIS, NIR, TIR)	>2000 km	250–1000 m	+ monitoring of broken ice zones
	Passive microwave radiometers	1500 km	12–25 km	+ ice concentration (open water fraction)
	Scatterometers	≥500 km	12–25 km	+ large-scale ice movement

the opportunity to combine data from imaging radar, multi-spectral instruments, and thermal radiometers. For polynya research, images from SAR systems operating at different frequencies and/or in polarimetric mode (such as TerraSAR-X, Radarsat-2, or ALOS-2 SAR), from high-resolution optical instruments (such as EO1-ALI or RapidEye), and from passive microwave radiometers such as AMSRE-2 are extremely useful as supplement to the Sentinel data.

Acknowledgments

The work of the first author was funded by the German Federal Ministry for Economic Affairs and Energy within the framework of project 50EE1217. The second author was partly supported by the project “Information content of multi-spectral SAR data”, ESA contract 4000115192/15/NL/AF/eg. The meteorological data and information for the AWS Eneide were obtained from ‘Meteo-Climatological Observatory’ of the Italian Programma Nazionale Di Ricerche in Antartide (PNRA). The authors appreciate the support of the University of Wisconsin-Madison Automatic Weather Station Program for the data set, data display, and information, NSF grant number ANT-1245663. EO-1 Data were obtained from the U.S. Geological Survey. SAR data from Envisat ASAR and ALOS PALSAR were provided by the European Space Agency, project ALO.3545, ALOS PALSAR imagery by the Japan Aerospace Exploration Agency (JAXA) within the frame of project 1098, and Envisat AATSR data by the European Space Agency. The authors would like to thank the two anonymous reviewers for their helpful and constructive suggestions and comments.

Appendix A. Supplementary data

Supplementary data associated with this article can be found in the online version at <http://dx.doi.org/10.1016/j.rse.2016.10.003>. These data include the Google map of the most important areas described in this article.

References

- Adams, S., Willmes, S., Schröder, D., Heinemann, G., Bauer, M., Krumpen, T., 2013. Improvement and sensitivity analysis of thermal thin-ice retrievals. *IEEE Trans. Geosci. Remote Sens.* 99. <http://dx.doi.org/10.1109/TGRS.2012.2219539>.
- Barber, D.G., Massom, R.A., 2007. The role of sea ice in Arctic and Antarctic polynyas. Chapter 1. In: Smith Jr., W.O., Barber, D.G. (Eds.), *Polynyas: Windows to the World*. Elsevier Oceanography Series 74, pp. 1–56.
- Bromwich, D.H., 1989. Satellite analyses of Antarctic katabatic wind behaviour. *Bull. Am. Meteorol. Soc.* 70 (7), 738–749.
- Casey, J.A., Howell, S.E., Tivy, A., Haas, C., 2016. Separability of sea ice types from wide swath C- and L-band synthetic aperture radar imagery acquired during the melt season. *Remote Sens. Environ.* 174, 314–328.
- Ciappa, A., Pietranera, L., 2013. High resolution observation of the Terra Nova Bay polynya using COSMO SkyMed X-SAR and other satellite imagery. *J. Mar. Syst.* 113–114, 42–51.
- Ciappa, A., Pietranera, L., Budillon, G., 2012. Observations of the Terra Nova Bay (Antarctica) polynya by MODIS ice surface temperature imagery from 2005 to 2010. *Remote Sens. Environ.* 119, 158–172.
- Comiso, J.C., Kwok, R., Martin, S., Gordon, A.L., 2011. Variability and trends in sea ice extent and ice production in the Ross Sea. *J. Geophys. Res.* Vol. 116, C04021. <http://dx.doi.org/10.1029/2010JC006391>.
- Corlett, G.K., Barton, I.J., Donlon, C.J., Edwards, M.C., Good, S.A., Horrocks, L.A., Llewellyn-Jones, D.T., Merchant, C.J., Minnett, P.J., Nightingale, T.J., Noyes, E.J., O'Carroll, A.G., Remedios, J.J., Robinson, I.S., Saunders, R.W., Watts, J.G., 2006. The accuracy of SST retrievals from AATSR: An initial assessment through geophysical validation against in situ radiometers, buoys and other SST data sets. *Adv. Space Res.* b (4), 764–769. <http://dx.doi.org/10.1016/j.asr.2005.09.037>.
- Darby, M.S., Willmott, A.J., Somerville, T.A., 1995. On the influence of coastline orientation on the steady state width of a latent heat polynya. *J. Geophys. Res.* 100 (C7), 13625–13633.
- Dierking, W., 2010. Mapping of different sea ice regimes using images from Sentinel-1 and ALOS synthetic aperture radar. *IEEE Trans. Geosci. Remote Sens.* 48 (3), 1045–1058. <http://dx.doi.org/10.1109/TGRS.2009.2031806>.
- Dierking, W., 2013. Sea ice monitoring by synthetic aperture radar. *Oceanography* 26 (2), 100–111. <http://dx.doi.org/10.5670/oceanog.2013.33>.
- Dierking, W., Busche, T., 2006. Sea ice monitoring by L-band SAR: an assessment based on literature and comparisons of JERS-1 and ERS-1 imagery. *IEEE Trans. Geosci. Remote Sens.* 44 (2), 957–970. <http://dx.doi.org/10.1109/TGRS.2005.861745>.
- Dierking, W., Dall, J., 2007. Sea ice deformation state from synthetic aperture radar imagery – part 1: comparison of C- and L-band and different polarizations. *IEEE Trans. Geosci. Remote Sens.* 45 (11), 3610–3622. <http://dx.doi.org/10.1109/TGRS.2007.903711>.
- Dierking, W., Dall, J., 2008. Sea ice deformation state from synthetic aperture radar imagery – part II: effects of spatial resolution and noise level. *IEEE Trans. Geosci. Remote Sens.* 46 (8), 2197–2207. <http://dx.doi.org/10.1109/TGRS.2008.917267>.
- Dokken, S.T., Winsor, P., Markus, T., Askne, J., Björk, G., 2002. ERS SAR characterization of coastal polynyas in the Arctic and comparison with SSM/I and numerical model investigations. *Remote Sens. Environ.* 80, 321–335.
- Drucker, R., Martin, S., Moritz, R., 2003. Observations of ice thickness and frazil ice in the St. Lawrence Island polynya from satellite imagery, upward looking sonar, and salinity/temperature moorings. *J. Geophys. Res.* 108 (C5), 3149. <http://dx.doi.org/10.1029/2001JC001213>.
- Drucker, R., Martin, S., Kwok, R., 2011. Sea ice production and export from coastal polynyas in the Weddell and Ross seas. *Geophys. Res. Lett.* 38, L17502. <http://dx.doi.org/10.1029/2011GL048668>.
- ESA, 2002. The AATSR Product Handbook. <http://envisat.esa.int/dataproducts/aatsr/>.
- Gallée, H., 1997. Air-sea interactions over Terra Nova Bay during winter: Simulations with a coupled atmosphere-polynya model. *J. Geophys. Res.* 102 (D12), 13835–13849.
- Haarpainter, J., Haugan, P.H., Gascard, J.-C., 2001. Interannual variability of the Storfjorden (Svalbard) ice cover and ice production observed by ERS-2 SAR. *Ann. Glaciol.* 33, 430–436.
- Hollands, T., Dierking, W., 2011. Performance of a multiscale correlation algorithm for the estimation of sea ice drift from SAR images: initial results. *Ann. Glaciol.* 52 (57), 311–317.
- Hollands, T., Haid, V., Dierking, W., Timmermann, R., Ebner, L., 2013. Sea ice motion at the Ronne Polynya, Antarctica: SAR observations versus model results. *J. Geophys. Res.* 118 (4), 1940–1954. <http://dx.doi.org/10.1002/jgrc.20158>.
- Hollands, T., Linow, S., Dierking, W., 2015. Reliability measures for sea ice motion retrieval from synthetic aperture radar images. *IEEE J. Sel. Top. Appl. Earth Obs. Remote Sens.* 8 (1), 67–75. <http://dx.doi.org/10.1109/JSTARS.2014.2340572>.
- Hunewinkel, T., Markus, T., Heygster, G.C., 1998. Improved determination of the sea ice edge with SSM/I data for small-scale analyses. *IEEE Trans. Geosci. Remote Sens.* 36 (5), 1795–1808. <http://dx.doi.org/10.1109/36718647>.
- Jardon, F.P., Vivier, F., Bourret-Aubertot, P., Lourenco, A., Cuypers, Y., Willmes, S., 2014. Ice production in Storfjorden (Svalbard) estimated from a model based on AMSR-E observations: impact on water mass properties. *J. Geophys. Res.: Oceans* 119, 377–393. <http://dx.doi.org/10.1002/2013JC009322>.
- Kern, S., 2009. Wintertime Antarctic coastal polynya area: 1992–2008. *Geophys. Res. Lett.* 36 (14), L14501. <http://dx.doi.org/10.1029/2009GL038062>.
- Kern, S., Spreen, G., Kaleschke, L., de la Rosa, S., Heygster, G., 2007. Polynya signature simulation method polynya area in comparison to AMSR-E 89 GHz sea ice concentrations in the Ross Sea and off the Adélie Coast, Antarctica, for 2002–05: first results. *Ann. Glaciol.* 46, 409–418.
- Key, J.R., Collins, J.B., Fowler, C., Stone, R.S., 1997. High-latitude surface temperature estimates from thermal satellite data. *Remote Sens. Environ.* 61 (2), 302–309. [http://dx.doi.org/10.1016/S0034-4257\(97\)89497-7](http://dx.doi.org/10.1016/S0034-4257(97)89497-7).
- Krumpen, T., Willmes, S., Morales Maqueda, M.A., Haas, C., Hölemann, J.A., Gerdes, R., Schröder, D., 2011. Evaluation of a polynya flux model by means of thermal infrared satellite estimates. *Ann. Glaciol.* 52 (57), 52–60.
- Long, D.G., Daum, D.L., 1998. Spatial resolution enhancement of SSM/I data. *IEEE Trans. Geosci. Remote Sens.* 36 (2), 407–417. <http://dx.doi.org/10.1109/36.662726>.
- Long, D.G., Stroeve, J., 2011. Enhanced-Resolution SSM/I and AMSR-E Daily Polar Brightness Temperatures. Ross Sea, Antarctica. Boulder, Colorado USA, NASA DAAC at the National Snow and Ice Data Center.
- Markus, T., Burns, B.A., 1995. A method to estimate sub-pixel-scale coastal polynyas with satellite passive microwave data. *J. Geophys. Res.* 100 (C3), 4473–4487.
- Martin, S., Drucker, R., Kwok, R., Holt, B., 2004. Estimation of thin ice thickness and heat flux for the Chuckchi Sea Alaskan coast polynya from special sensor microwave/imager data, 1990–2001. *J. Geophys. Res.* 109, C10012. <http://dx.doi.org/10.1029/2004JC002428>.
- Martin, S., Drucker, R., Kwok, R., Holt, B., 2005. Improvements in the estimation of ice thickness and production in the Chuckchi Sea polynyas derived from AMSR-E. *Geophys. Res. Lett.* 32, L05505. <http://dx.doi.org/10.1029/2004GL022013>.
- Massom, R.A., Hill, K.L., Lytle, V.I., Worby, A.P., Paget, M., Allison, I., 2001. Effects of regional fast ice and iceberg distributions on the behavior of the Mertz Glacier Polynya, East Antarctica. *Ann. Glaciol.* 33, 391–398.
- Mathew, N., Heygster, G., Melsheimer, C., Kaleschke, L., 2008. Surface emissivity of Arctic sea ice at AMSU window frequencies. *Trans. Geosci. Remote Sens.* 46 (8), 2298–2306.
- Morelli, S., Parmiggiani, F., 2013. Wind over TerraNova Bay (Antarctica) during a polynya event: Eta model simulations and satellite microwave observations. *Eur. Phys. J. Plus* 128, 135. <http://dx.doi.org/10.1140/epjp/i2013-13135-8>.
- Nakamura, K., Wakabayashi, H., Naoki, K., Nishio, F., Moriyama, T., Uratsuka, S., 2009. Observation of sea-ice thickness in the sea of Okhotsk by using dual-frequency and fully polarimetric airborne SAR (Pi-SAR) data. *IEEE T. Geosci. Remote Sens.* 43, 2460–2469.
- Plueddemann, A.J., Smith, J.A., Farmer, D.M., Weller, R.A., Crawford, W.R., Pinkel, R., Vagle, S., Gnanadesikan, A., 1996. Structure and variability of Langmuir circulation during the surface waves processes program. *J. Geophys. Res.* 101, 3525–3543.
- Preußer, A., Willmes, S., Heinemann, G., Paul, S., 2015. Thin ice dynamics and ice production in the Storfjorden polynya for winter seasons 2002/2003–2013/2014 using MODIS thermal infrared imagery. *Cryosphere* 9, 1063–1073. <http://dx.doi.org/10.5194/tc-9-1063-2015>.
- Pringle, D.J., Eicken, H., Trodahl, H.J., Backstrom, L.G.E., 2007. Thermal conductivity of landfast Antarctic and Arctic sea ice. *J. Geophys. Res.* 112, C04017. <http://dx.doi.org/10.1029/2006JC003641>.

- Rusciano, E., Budillon, G., Fusco, G., Spezie, G., 2013. Evidence of atmosphere-sea ice-ocean coupling in the Terra Nova Bay polynya (Ross Sea – Antarctica). *Cont. Shelf Res.* 61–62, 112–124.
- Shokr, M., Sinha, N.K., 2015. *Sea Ice: Physics and Remote Sensing*, Geophysical Monograph 209, AGU, Wiley Chapter 8.4. pp. 373–381.
- Tamura, T., Ohshima, K.I., Nihashi, S., 2008. Mapping of sea ice production for Antarctic coastal polynyas. *Geophys. Res. Lett.* 35, L07606. <http://dx.doi.org/10.1029/2007GL032903>.
- Thorpe, S.A., 2004. Langmuir circulation. *Annu. Rev. Fluid Mech.* 36, 55–79.
- Torres, R., et al., 2012. GMES Sentinel-1 mission. *Remote Sens. Environ.* 120, 9–24. <http://dx.doi.org/10.1016/j.rse.2011.05.028>.
- Toyota, T., Nakamura, K., Uto, S., Ohshima, K.I., Ebuchi, N., 2009. Retrieval of sea ice thickness distribution in the seasonal ice zone from airborne L-band SAR. *Int. J. Remote Sens.* 30, 3171–3189.
- Van Woert, M.L., 1999. Wintertime dynamics of the Terra Nova Bay Polynya. *J. Geophys. Res.* 104 (C4), 7753–7769.
- Wakabayashi, H., Matsuoka, T., Nakamura, K., 2004. Polarimetric characteristics of sea ice in the Sea of Okhotsk observed by airborne L-band SAR. *IEEE T. Geosci. Remote Sens.* 42, 2412–2425.
- Williams, W.J., Carmack, E.C., Ingram, R.G., 2007. Physical oceanography of polynyas, chapter 2. In: Smith Jr., W.O., Barber, D.G. (Eds.), *Polynyas: Windows to the World*. Elsevier Oceanography Series 74, pp. 55–85.
- Willmes, S., Krumpen, T., Adams, S., Rabenstein, L., Haas, C., Hoelemann, J., Hendricks, S., Heinemann, G., 2010. Cross-validation of polynya monitoring methods from multisensor satellite and airborne data: a cases study for the Laptev Sea. *Can. J. Remote. Sens.* 36 (Suppl. 1), S196–S210.
- Willmes, S., Adams, S., Schroeder, D., Heinemann, G., 2011. Spatiotemporal variability of sea-ice coverage, polynya dynamics and ice production in the Laptev Sea between 1979 and 2008. *Polar Res.* 30, 5971. <http://dx.doi.org/10.3402/polar.v30i0.5971>.
- Willmott, A.J., Holland, D.M., Morales Maqueda, M.A., 2007. Polynya modelling, chapter 3. In: Smith Jr., W.O., Barber, D.G. (Eds.), *Polynyas: Windows to the World*. Elsevier Oceanography Series 74, pp. 87–126.
- Yu, Y., Lindsay, D.A., 1996. Thin ice thickness from satellite thermal imagery. *J. Geophys. Res.* 101 (C10), 25753–25766.